Consequences of thermite welding on the microstructure of the heat affected zone of a carbide-free bainitic steel rail

T. Lesage, M.N. Avettand-Fènoël, M. Masquelier, Frederic Danoix, L. Kamgaing

Consequences of thermite welding on the microstructure of the Heat Affected Zone of a carbide-free bainitic steel rail

T. Lesage[1-2*], M.N. Avettand-Fènoël[2], M. Masquelier[2], F. Danoix[3], L. Kamgaing[4]

[1] Institut de Recherche Technologique RAILENIUM, F-59300, Famars, France
[2] Univ. Lille, CNRS, INRAE, Centrale Lille, UMR 8207- UMET - Unité Matériaux Et Transformations, 59000 Lille, France
[3] Normandie Université, UNIROUEN, INSA Rouen, CNRS, Groupe de Physique des Matériaux, 76000 Rouen, France
[4] Saarstahl Rail, 164 rue du Maréchal Foch, BP 10166, 57705 Hayange Cedex, France
**Corresponding author : thibault.lesage@railenium.eu*

Abstract

Due to their excellent Rolling Contact Fatigue (RCF) resistance, Carbide-Free Bainitic (CFB) steels rails have recently received increasing attention to replace pearlitic steels in the railways sector. This is mainly attributed to the TRansformation Induced Plasticity (TRIP) effect, which mechanically transforms austenite into martensite during wheel/rail contact. However, the welding of these carbide-free bainitic steels could lead to a local decrease in mechanical properties, as well as RCF resistance, inside the Heat Affected Zone, which limits the use of these steels. The present work aims to explain the reason of the loss of RCF resistance of these steels after welding. To do so, the microstructure evolution along the Heat Affected Zone is investigated thoroughly, and is linked with its thermal history. In the most critical areas in terms of RCF resistance, the consumption of all retained austenite has been evidenced, thus suppressing TRIP effect. This loss of austenite is mainly observed in a critical range of temperatures and has been linked to the low thermal stability of austenite. The microstructural investigations performed lead to a proposal of improvements in terms of rail chemical composition and/or heat treatments, in such a way that carbide-free bainitic steels rails could be less sensitive to RCF resistance loss after welding.

Keywords: Rolling Contact Fatigue, Carbide-free bainitic steel, Welding, Microstructure, Stability of austenite, Railways

1. Introduction

Mechanical solicitation in railway applications has become more and more critical as the train tonnage increased over the years. The tracks are subjected to high stresses that cause rail damage, including cracks which could eventually lead to fracture of rails [1]. This causes serious safety issues and great maintenance costs. Thus, rail optimization is required to increase safety and rail lifetime. Pearlitic rails, such as R260, R350HT and R370CrHT grades, have been commonly used in European railways over the past decades [2–4]. These grades present vast advantages but are prone to Rolling

Contact Fatigue (RCF), and more specifically to Head Check (HC) defects [2]. HC defects are cracks found at the gauge corner of the outer rail, usually clustered at uniform intervals. Most of these HC defects are found in curved tracks in tight curves (radii less than 3000 m), as well as in switches and crossings [5]. These pearlitic steel rails have been extensively studied over the years; however, the mechanical properties of these steels are believed to be close to their theoretical limit with current chemistries and processing techniques [2]. An alternative solution to partially replace pearlitic steel rails is Carbide-Free Bainitic (CFB) steel rails. These rails present outstanding RCF resistance, and are now receiving increasing interest [3,6,7].

During rail solicitation, the sub-surface microstructure of the rail is significantly altered. Microstructure refinement is typically observed in this region. In pearlitic rails, a loss of the pearlitic nodules structures and cementite dissolution is observed under shear stress, eventually leading to cracking [8–10]. Conversely, in CFB steel grades, most of the microstructural change is located in the retained austenite. Once the strain that can be accommodated by austenite becomes too high, it partially transforms into martensite, following the TRansformation Induced Plasticity (TRIP) effect. This TRIP effect creates a compressive stress that delays microvoid nucleation inside austenite. This plays a vital role in enhancing the total elongation of bainitic steels [11–13]. It also enables crack tip closure, therefore retarding crack propagation [14–16]. Furthermore, this transformation consumes most of the energy resulting from mechanical straining, hereby reducing the available energy for fatigue crack growth [17–19]. Crack growth rate is lowered and RCF resistance is increased. As a result, the high RCF resistance of these CFB grades is associated with the TRansformation Induced Plasticity (TRIP) effect [20–22]. Consequently, these steels are also known as TRIP-aided bainitic ferrite steels [23] or super-bainitic TRIP steels [24]. TRIP steels are widely used in the automotive industry [25–29] but have only recently been studied in the railways industry. In addition to the TRIP effect, as indicated in a previous work performed by the authors [21], the elevated RCF resistance of CFB steels can be related to the combination of a low fatigue crack growth rate with a high wear rate observed in these steels. It results in a “self-grinding” steel, where the cracked layer in close surface gets worn away faster than the cracks develop. This high wear rate also leads to the emergence of a microstructure formerly located deeper inside the material, less impacted by the solicitation, with therefore more untransformed austenite available.

Despite all these advantages, some difficulties arise with CFB when it comes to welding. For CFB rails, the most common welding processes are flash butt welding and thermite welding [30]. Thermite welding is fast and cost-efficient while maintaining a satisfactory quality [30,31]. However, it is as or even more susceptible to stress concentration than flash butt welding, making it more sensitive to fatigue defects [30,32]. Welding defects can be divided in two main categories: geometrical discontinuities and material discontinuities [33]. Most of geometrical discontinuities originate from misalignments or grinding problematics and are inherent to welding process. Material discontinuities

encompass mainly hardness variation, microstructural gradient, inclusions or voids in the weld metal, porosity and residual stress [33–35]. Residual stress is especially critical in both structural performances and RCF resistance [36,37]. Some supplementary issues may arise from the grinding operation occurring after welding, which may cause white etching layers [38], martensite transformation or geometrical defects. All these defects may induce crack, either located inside the Solidified Zone (SZ), or, more frequently, inside the Heat Affected Zone (HAZ) or at the interface between HAZ and SZ [39]. Up to 60%-80% of rails failures in welded bainitic steels occur inside the HAZ [34,37]. Cracks usually initiate in the rail head due to wheel/rail contact, especially in presence of welding defects, and propagates through the head, web and foot [40–43]. During rail service, any of the previously discussed discontinuities lead to either an increase in local stress or a degradation of mechanical properties [33]. Eventually, rail fatigue life is reduced and the weld (SZ or HAZ) becomes a weak spot. RCF is one of the main causes of defects and failure and is considered herein. Field investigations indicated that no RCF defect could be found in the Base Material (BM) of these steel grades. However, some cases of RCF defects, and especially Head Check defects, have been observed in service [44] for this grade close to thermite welds. Most of these defects initiated inside the HAZ rather than inside the SZ itself, as typically seen in Figure 1.

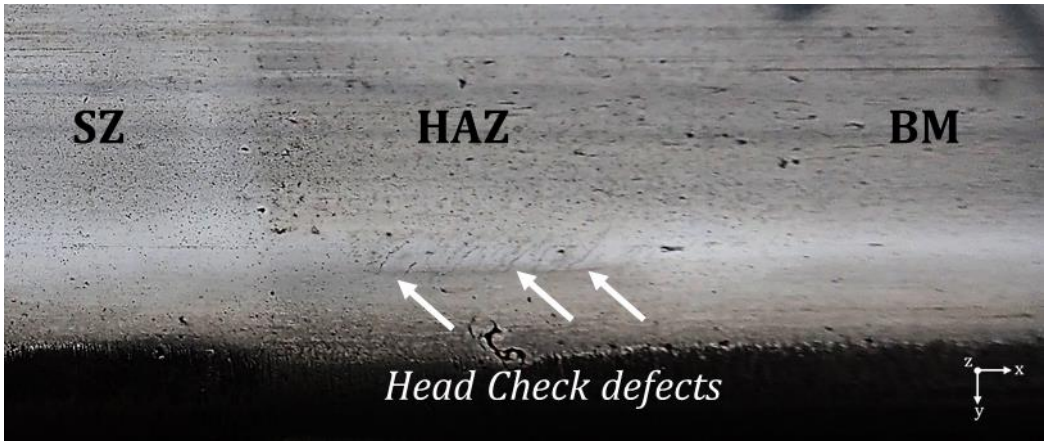

Figure 1: Typical Head Check defects observed inside HAZ of a CFB rail after service. No macroscopic defect is detected in neither SZ nor BM.

This work aims to investigate ways to improve current RCF resistance of CFB HAZ, focusing on the rail perspective. The HAZ of CFB rails is investigated in details, while the SZ is not studied extensively. Prior work by the authors [21] emphasized that the elevated RCF resistance in BM of these steels is mainly attributed to the austenitic transformation into martensite *via* TRIP effect. Consequently, the stability and phase content evolution of austenite phase along the HAZ will be carefully investigated. Since all defects noticed in service are RCF defects, a focus is made on close surface investigations at 10 mm from the rail head surface or less. To better understand the microstructures observed, the thermal history of the HAZ is also characterized, using thermocouple inserted inside the HAZ. This experimental work is backed up by a modelling part of the thermal history, whose main objective is to extend the data

obtained in localized positions to the rest of the HAZ. Finally, using the microstructural conclusions drawn, several improvements of current CFB steel rail's HAZ are proposed.

2. *Materials and methods*

2.1. Initial rails

The rails were processed by Saarstahl Rail (France) using initial rectangular section bars (blooms) heated up to 1100°C, hot rolled at 960°C and air cooled down up to room temperature with a cooling rate of about 0.15°C/s. These blooms were then shaped into Vignole rails with initial 60E2 profile. The chemical composition of the rail selected during this study is indicated in Table 1. For these CFB steels, the formation of cementite is suppressed by the addition of silicon [45–47].

Table 1: Chemical composition intervals (in wt.%) of the considered bainitic steel as indicated by Saarstahl Rail. The composition of the solidified zone or the Fusion Zone, as commonly called in the welding community, is provided by Pandrol

Zone considered	C	Mn	Si	Cr	S	P	Fe
Base material	0.2 - 0.4	1.2 - 1.8	0.8 - 1.8	0.3 - 0.8	≤ 0.025	≤ 0.025	Bal.
Solidified zone	0.1 – 0.3	0.3 – 0.5	1.6 - 2.2	2.2 – 2.6	≤ 0.025	≤ 0.025	Bal.

Table 2 indicates the melting temperature (MT), austenite finishing (Ac3) and austenite starting (Ac1), Martensite start (Ms) and Bainitic start (Bs) temperatures, as provided by Saarstahl Rail steel manufacturer.

Table 2: Mechanical and thermal properties of the studied CFB steel, as provided by Saarstahl Rail.

Thermal properties	**MT (°C)**	**Ac3 (°C)**	**Ac1 (°C)**	**Ms (°C)**	**Bs (°C)**
Base Material	1530	877	745	345	442
Mechanical properties	**Rm (MPa)**	**Elongation (%)**		**Hardness ($HV_{0.05}$)**	
Base Material	> 1200	> 13		340 ± 10	

Studied carbide-free bainitic microstructure in base material is indicated in Figure 2. It consists mainly of bainitic ferrite (blue-colored in Figure 2.b), austenite (red-colored in Figure 2.b), as well as Martensite-Austenite Compound (MAC) (darker area in Figure 2.b).

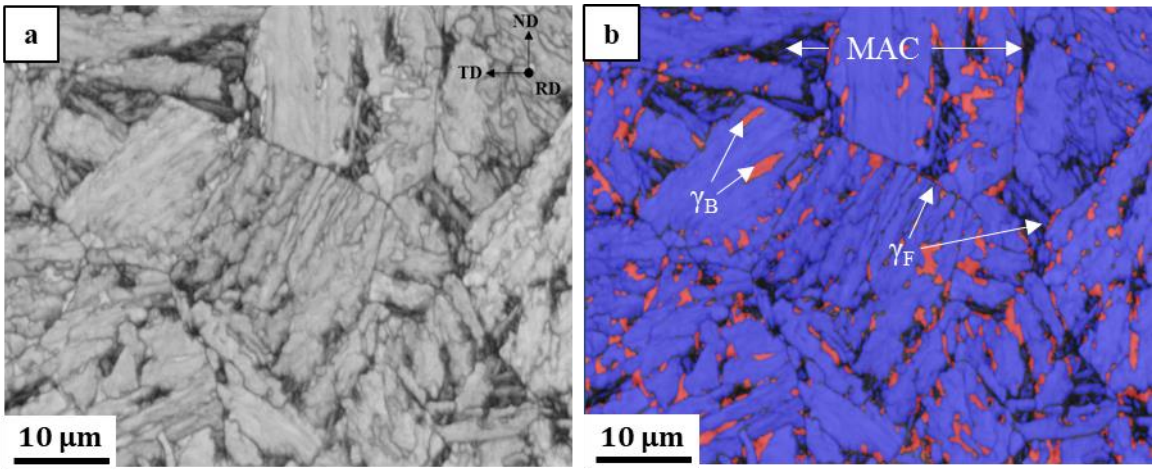

Figure 2: Initial microstructure of the CFB steel grade observed by EBSD. a- band contrast; b -phase map superimposed with band contrast. Bainitic ferrite (BCC phase) is blue-colored, austenite is colored in red.

Inside CFB steels, two shapes of austenite are to be found: austenitic block (γ_B) and austenitic film (γ_F). Austenitic film γ_F (Figure 3.a) is, as its name suggests, elongated, with typical dimensions in the order of a few dozen of nanometers wide and up to one micrometer long. It is characterized by a high carbon content and is mainly located between bainite sub-units or at Prior Austenite Grain Boundaries (PAGB) [48–51]. Austenitic block γ_B (Figure 3.b) is coarser than films and somewhat equiaxed. It presents a radius ranging from a few hundreds of nanometers to a few micrometers [52], and is mainly observed between the sheaves of bainite [48,53].

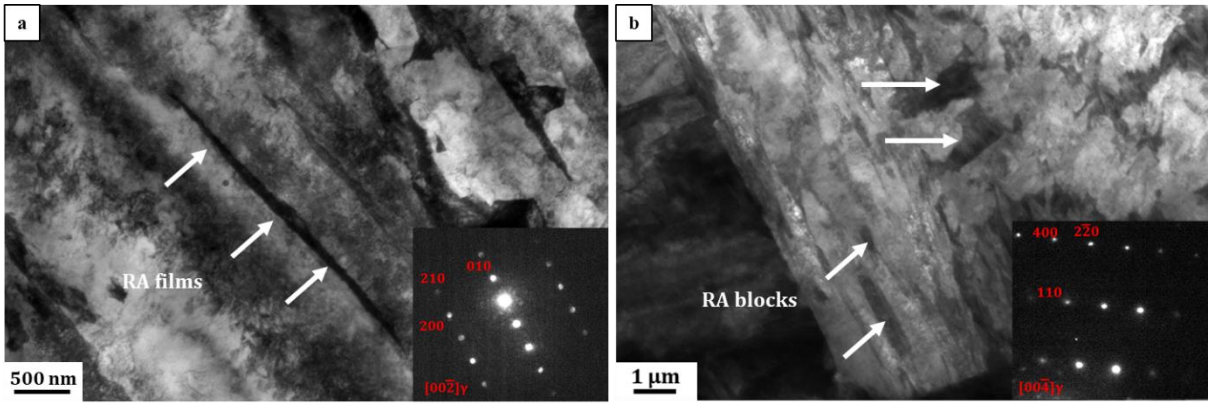

Figure 3: Bright field transmission electron micrographs along with corresponding Selected Area Diffraction Pattern (SADP) exhibiting a- Film-like retained austenite (RA) and b- blocky retained austenite. Retained austenite is indicated by white arrows in both images.

2.2. Thermite welding

2.2.1. Process

Thermit welding is based on an exothermic chemical reaction, which involves the reduction of a metal oxide, usually iron oxide, by aluminum, as shown in the equation (1) [54].

$$Fe_2O_3 + 2\ Al \rightarrow Al_2O_3 + 2\ Fe + \textit{heat} \quad (1)$$

During the ignition, temperatures generated by the reaction can go up to more than 2700°C [31,55], leading to temperatures higher than 2000°C [34,56] once the liquid metal is poured inside the mold. Industrial thermite welding process is performed by Pandrol and consists of five different steps:

- Preheating at 850°C for 6 min (Figure 4.a) between the rails to be welded. The initial gap between both rails is 25±1 mm wide.
- Casting of the portion (Figure 4.b), estimating an initial temperature of 2200°C.
- Cooling with a sand mold surrounding the welded area (Figure 4.c).
- Removal of the vent risers (Figure 4.d) after 3 min.
- Natural cooling (Figure 4.e).

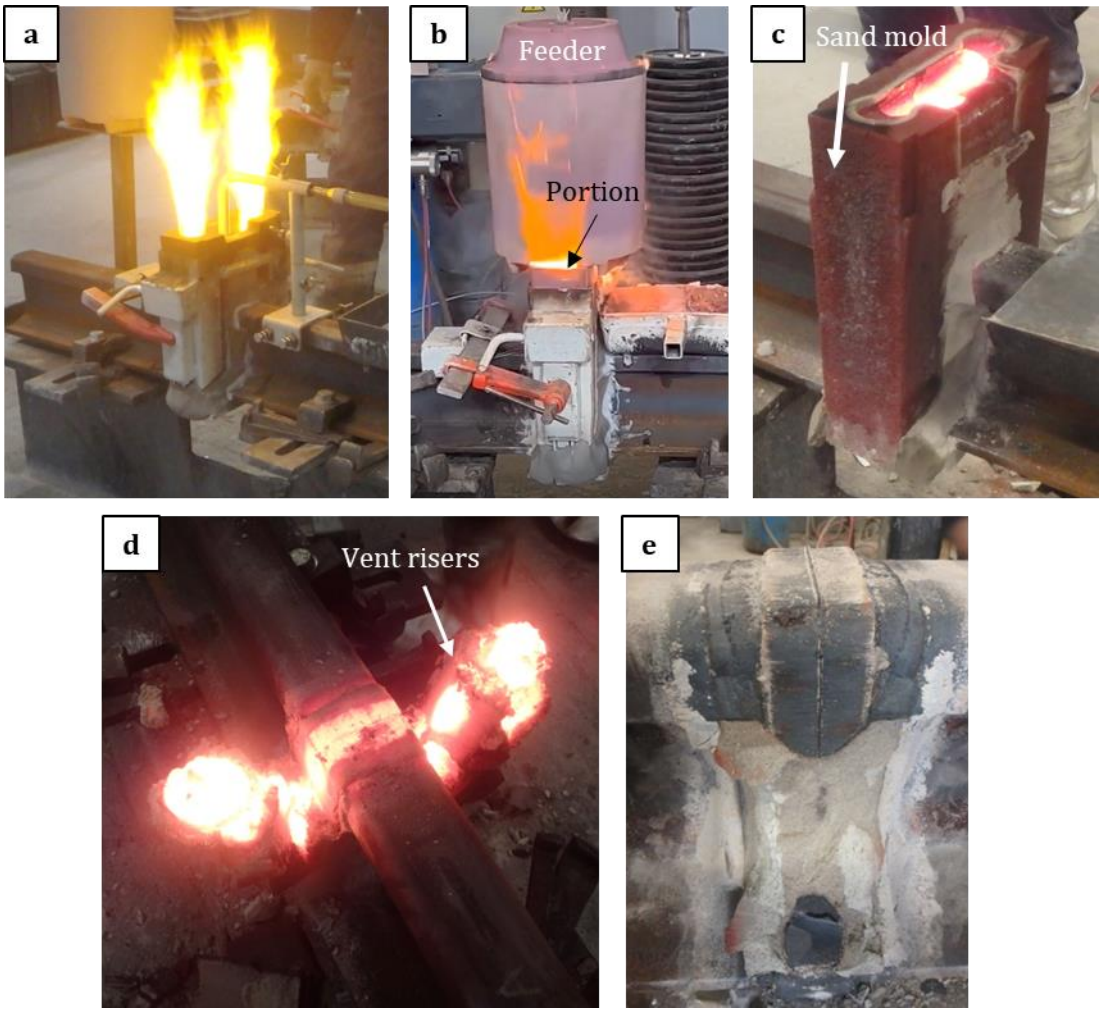

Figure 4: Thermite welding process steps: a- Preheating, b- Casting c- Cooling with sand mold and feeder, d- removal of the feeder and e- natural cooling

Once cooling is finished, welded rail is properly ground to recover the initial 60E2 profile. The welding process leads to the formation of distinct regions: the Solidified Zone (SZ), also called Fusion Zone in the welding community, the HAZ surrounding it, and the Base Material (BM), unaffected by the welding process. In the following, the HAZ is defined as the whole region in the vicinity of the solidified zone where microstructural modifications are to be observed. Thus, it does also include regions where maximum temperature reached is low compared to Ac1, if any microstructural modification is observed, which corresponds to the case of steel tempering.

2.3. Characterization techniques

Hardness measurements were performed using a Buehler Micromet 5100 series with a Vickers indenting head using a 0.05 N load. Hardness profiles were performed following x direction on cross secitons at a depth of 1 mm from the running surface. The use of a small load allows measurements every 100 µm which enables a good enough accuracy to follow the microstructural evolution. Each measure is repeated 10 times for repeatability considerations.

For microstructural characterization techniques, systematic polishing was performed using grid papers grad 180, 300, 500, 800, 1200, 2400, followed by finish polishing using 6 µm, 3 µm, 1 µm and ¼ µm diamond paste. For light microscopy (OM) and scanning electron microscopy (SEM) investigations, this metallographic preparation was followed by etching, using a solution of 5% picric acid with 0.5% HCl in ethanol for 10 sec for base material, and Fry's etchant (15% HCl + 0.5% $CuCl_2$ diluted in 55% distilled water and 24.5% ethylic alcohol) for 30 sec for HAZ observation.

For electron back scattered diffraction (EBSD) analyses, finish polishing was followed by mechanical polishing using VibroMet 2 vibratory polisher. A solution of 30% Oxide Polishing Suspension (OPS) with colloidal silica – 70 % ethylic alcohol was used at 100% vibration for 1 hour followed by 36 hours at 10% vibration.

Observations were performed with a light Microscope Zeiss Axioplan, as well as a Hitachi $SU5000^R$ scanning electron microscope (SEM) with secondary electron (SE) and backscattered electron (BSE) modes. Energy Dispersive X-ray analysis (EDX) was used for chemical identification at a microscopic scale, with a 15 kV acceleration voltage and an acquisition time of 15 s. Electron BackScatter Diffraction (EBSD) was performed to have crystal orientations at the micrometric and submicrometric scales, using a 25 kV acceleration voltage. Aztec software (6.1) was used for EDX and EBSD acquisition. Step size is fixed at 80 nm.

During EBSD investigation, bainite and austenite content are directly determined by Aztec software. Despite the Body-Centered Tetragonal (b.c.t.) nature of indexed martensite, the low carbon atomic content of martensite, that is 0.3 at%, as measured later in Section 4.1), leads to a low tetragonality of this phase, which induces a lattice parameters ratio c/a close to 1. As a result, Body-Centered Cubic (b.c.c.) indexing is the most efficient way to detect martensite. Thus, b.c.c. indexing indicates both bainite and martensite content together, and, in some rare cases, ferrite. To differentiate between both phases, image analyses are performed by ImageJ on band contrast maps. The lower index quality of martensite, not being an actual b.c.c phase, makes it darker on band contrast maps, which allows its indexing. Conversely, ferrite is better indexed, which makes it recognizable after image analyses on band contrast maps.

Phase maps are superimposed with band contrast to account for the presence of martensite or, in some cases, ferrite (lighter blue on the image due to a better indexing). All of the phase maps shown are presented with austenite in red, bainite, ferrite and martensite in blue and Fe_3C in yellow.

X-Ray Diffraction (XRD) analyses were performed for phase quantification with a Diffractometer X'Pert Pro from Philips-Panalytical in Bragg-Brentano configuration, using a Kα cobalt wavelength at 0.1789 nm with a Kβ iron filter. It is used complementary to EBSD for austenite indexation. EBSD resolution (80 nm), is high enough to correctly index all austenite blocks, whose diameter is in the order of the micrometer. However, not all austenite films are detected by EBSD, due to their width of 30nm-150nm. Since EBSD allows the quantification of austenite blocks but only part

of films, austenite film content is approximated as the subtraction between austenite content indexed by XRD with austenite block content indexed by EBSD.

Thin foils for Transmission Electron Microscopy (TEM) were obtained by mechanically grinding of thin sections up to a thickness of 50-100 µm. Electropolishing was carried out using a solution of 5 vol.% perchloric acid – 95 vol% methanol. Struers TenuPol 5 was used for electropolishing, using a voltage of 15 V. Solution was kept below 5°C, with a current density close to 750 mA/cm².

Observations of the microstructure at nanoscale were carried out using a FEI G2000 Tecnai instrument, with a Field Electron Gun (FEG) electron source. Additionally, a ThermoFisher TITAN Themis 60–300 microscope equipped with a probe aberration corrector, operated at 200 kV, was used to acquire (high-resolution) scanning TEM ((HR)STEM) images. Probe size was set to 0.1 nm with a convergence semi-angle of 22.5 mrad. Collection angles of the high angle annular dark-field (HAADF) detector were set in the range of 80–150 mrad, as described in Ma *et al.* [57].

Finally, Atom Probe Tomography (APT) investigations were carried out on a CAMECA LEAP 4000 HR system operating in voltage mode at 50 K, with a pulse fraction of 20% and a repetition rate of 200 kHz, as described in Pushkareva *et al.* [58].

3. Results

3.1. Heat Affected Zone regions

During thermite welding, a HAZ of several centimeters is produced (Figure 5). Depending on the maximum temperature reached and the cooling history in the HAZ, microstructure changes are to be expected along this zone. Chemical etching and hardness evolution have been performed inside the HAZ. These techniques can be used to distinguish 5 areas in the HAZ, namely the Solidified Zone (SZ), Fine Grain (FG) and Coarse grain (CG), InterCritical (IC) and SubCritical (SC) areas. Figure 5 depicts a clear distinction between the Solidified Zone (SZ) and the Coarse Grain (CG) zone. The limit between IC ($Ac1 < T_{max} < Ac3$) and SC ($T_{max} < Ac1$) zones is also initially identified by the existence of a greenish area (highlighted by a white arrow in Figure 5), hinting a peculiar microstructure. This will be confirmed by the modelling described in Section 3.3. The position of Ac3 isotherm could not be determined by etching alone but will be determined later on by thermocouples measurements as well as modelling. Its position has been added to Figure 5 to ease the readability of the present article.

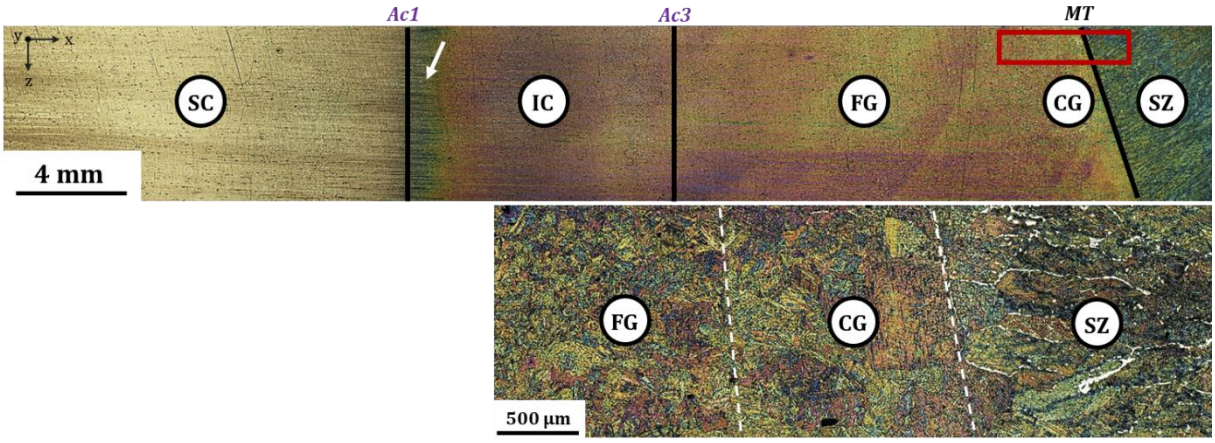

Figure 5: HAZ microstructure observed by optical microscopy after Fry etching for 30 s. The top of the figure corresponds to the surface of the rail. The white arrow indicates a peculiar microstructure close to Ac1 temperature. The picture enclosed in red corresponds to a zoom of CG region to better estimate its dimensions compared to FG region.

These macroscopic investigations have been coupled with hardness profile to have a first glance of the effect of thermal history on mechanical properties inside HAZ (Figure 6). Hardness measurements were performed in cross section at a 1 mm depth in order to be at the same depth as future EBSD investigations. In this figure, the hardness measured the furthest away from the SZ does not match BM's hardness, which indicates that the HAZ is more than 80 mm long (x > 130 mm). HAZ continues further for a few millimeters but no measurements were performed up to this point.

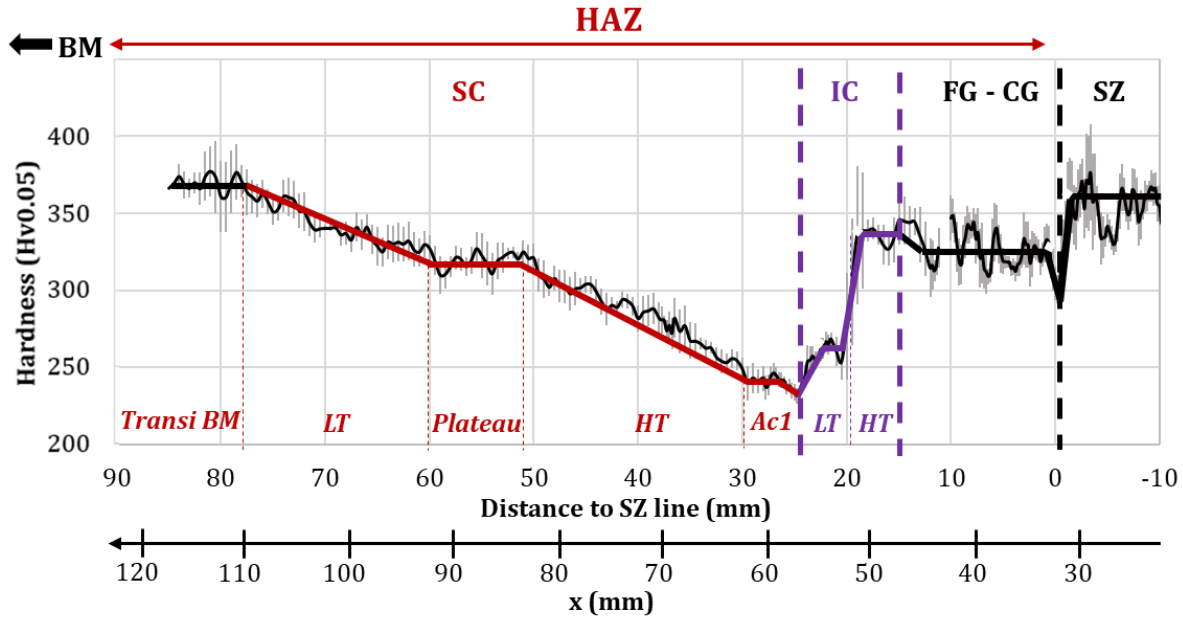

Figure 6: Hardness profile along the HAZ, measured in cross section a 1 mm depth from the top surface with error bars in grey. The relative position 0 corresponds to the limit between HAZ and SZ. x axis is indicated below the distance to SZ line. The general tendency of this hardness profile is highlighted by black (SZ, FG and CG regions), purple (IC region) and red (SC region) full lines.

3.2. Thermal history determination

3.2.1. Thermal cycles recorded by thermocouples

In CFB steels, the initial presence of austenite, is primordial to obtain a good RCF resistance. Since the maximum temperature reached during welding is high compared to Ac3, novel austenite is to be formed close to the weld. The position where the temperature peak exceeds Ac1 and Ac3 is thus important to determine since it will influence the nature, size, distribution, and possibly chemical composition of austenite. To determine these positions and accurately characterize the HAZ, a dual approach has been performed, using both modelling and experimental investigations *via* thermocouples insertion inside the rail to be welded. The use of modelling allows to have an overview of the global HAZ and thus to extend the local measurements performed experimentally.

To characterize experimentally the HAZ, several thermocouples have been inserted into the rail. Figure 7 indicates the coordinate system used in this study. The reference position is taken in such a way that:

- x = 0 refers to the middle of the weld seam
- y = 0 refers to the middle of the running band
- z = 0 refers to the surface of the rail head

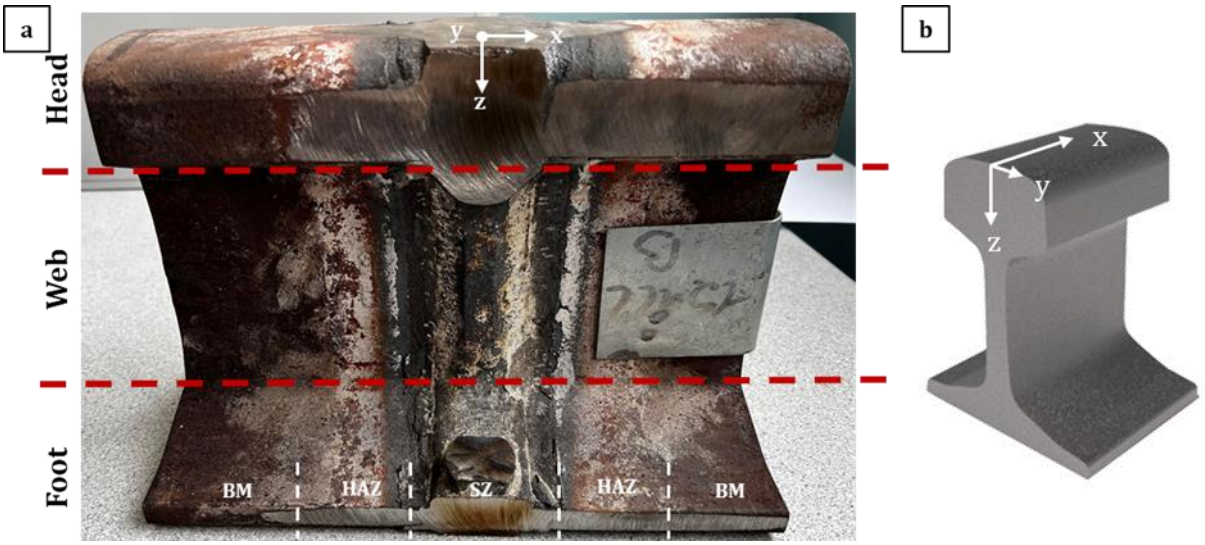

Figure 7: a- Picture of the welded rail with XYZ coordinates after cutting operation. The different regions (Solidified Zone, Heat Affected Zone and Base Material) are indicated in the bottom of the image. b- scheme of the rail in 3D view with XYZ coordinate system.

For the experimental characterization, Inconel600 thermocouples K of 1 mm diameter, with a melting point of 1415°C have been inserted into the rail at different positions of the HAZ (Figure 8.a). Picolog software was used to record the data during welding. Each rail portion to be welded is 1m10 long (x direction), with a width of 72 mm (y direction) and a depth of 172 mm (z direction). All investigations were performed in the rail head (z < 50 mm), where RCF defects are likely to occur. Since this study focuses on RCF resistance, the depth selected is kept low in front of rail dimensions to obtain surfacic or close-surface data. Cylindrical holes have been drilled following the x direction) as to insert thermocouples which will be located in the middle of the running surface (y = 0). To account for the influence of depth, thermocouples are placed at two distinct depths: z = 1 mm (thermocouples A and C) and z = 10 mm (thermocouple B and D). Each pair of thermocouples is separated by 10 mm from each

other ($x_{A,B}$ = 33mm and $x_{B,D}$ =43 mm). The configuration and position of the thermocouples are presented in Figure 8.a. To determine the most relevant position to insert thermocouples in x direction, a preliminary weld has been performed (Figure 8.b) on a similar CFB steel rail. Welded rail has then been etched to estimate roughly the position of the border between the SZ and the HAZ and Ac1 isothermal position. Using the dimensions of the weld seam observed after the preliminary test (Figure 8.b), thermocouples were placed inside the zone which will become the HAZ after welding (Figure 8.c). The indicated coordinates correspond to the tip position. The position of the thermocouples in y = 0 is represented in Figure 8.c and summed up in Figure 8.d. Thermocouple X was placed as close as possible to the weld seam. However, due to the poor repeatability of the dimensions of the seam, thermocouple X ended inside the weld seam. Since its fusion temperature is lower than CFB's ($MT_{thermocouple}$ = 1415°C while MT_{CFB} = 1530°C), the thermocouple melt and its data recorded were not exploitable.

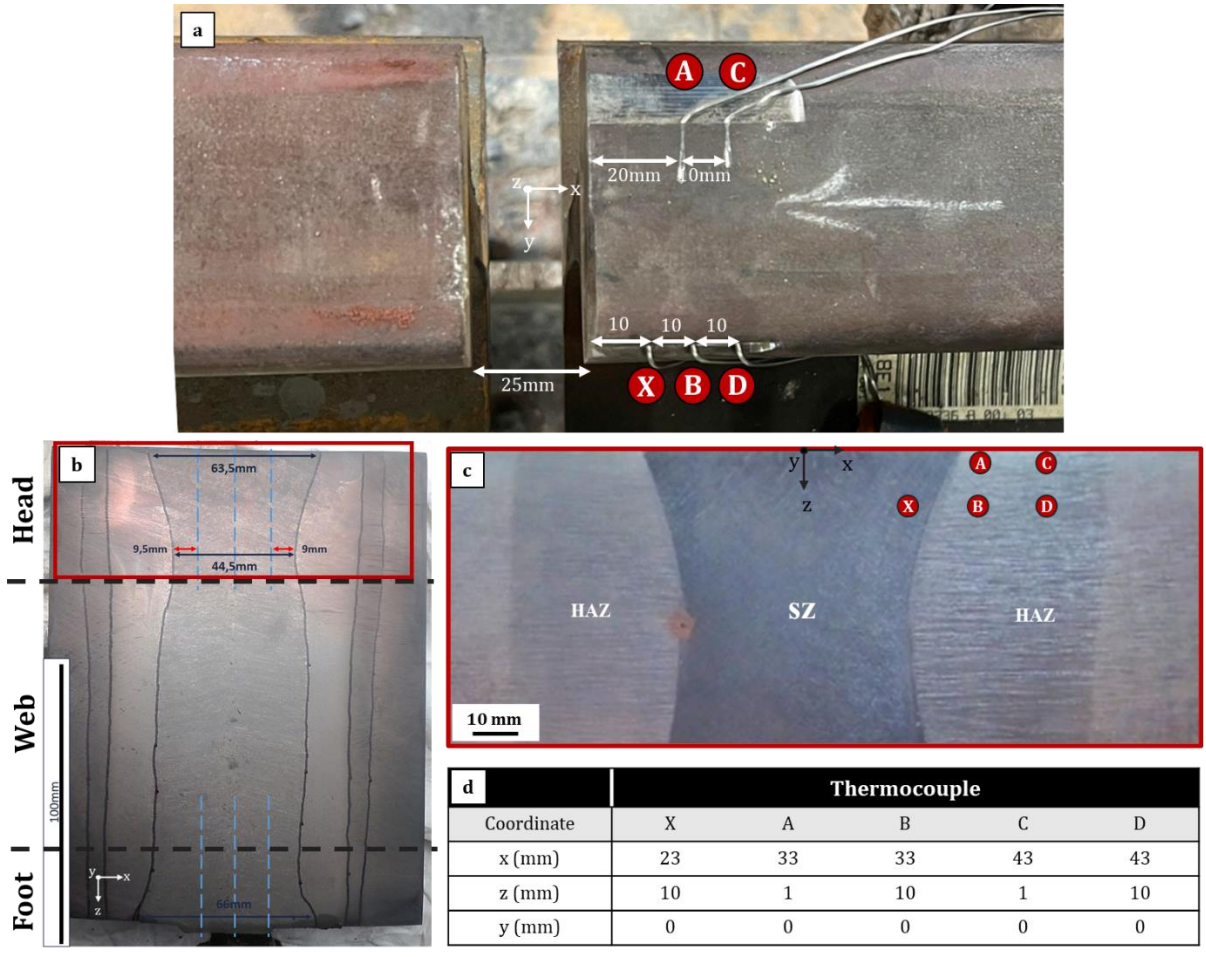

d	Thermocouple				
Coordinate	X	A	B	C	D
x (mm)	23	33	33	43	43
z (mm)	10	1	10	1	10
y (mm)	0	0	0	0	0

Figure 8: a- Welding set up with the inserted thermocouples b- Weld sample after preliminary test etched to reveal the dimensions and shape of the weld seam. c- close up of the etched rail head resulting from the second welding process. The position of the four thermocouples studied (named A to D) is represented on this figure. Thermocouple X melted and its data is therefore not presented. d- synthesis of the coordinates of each four thermocouples.

Figure 9 displays the recorded thermal cycles and cooling speed for all four thermocouples (A to D).

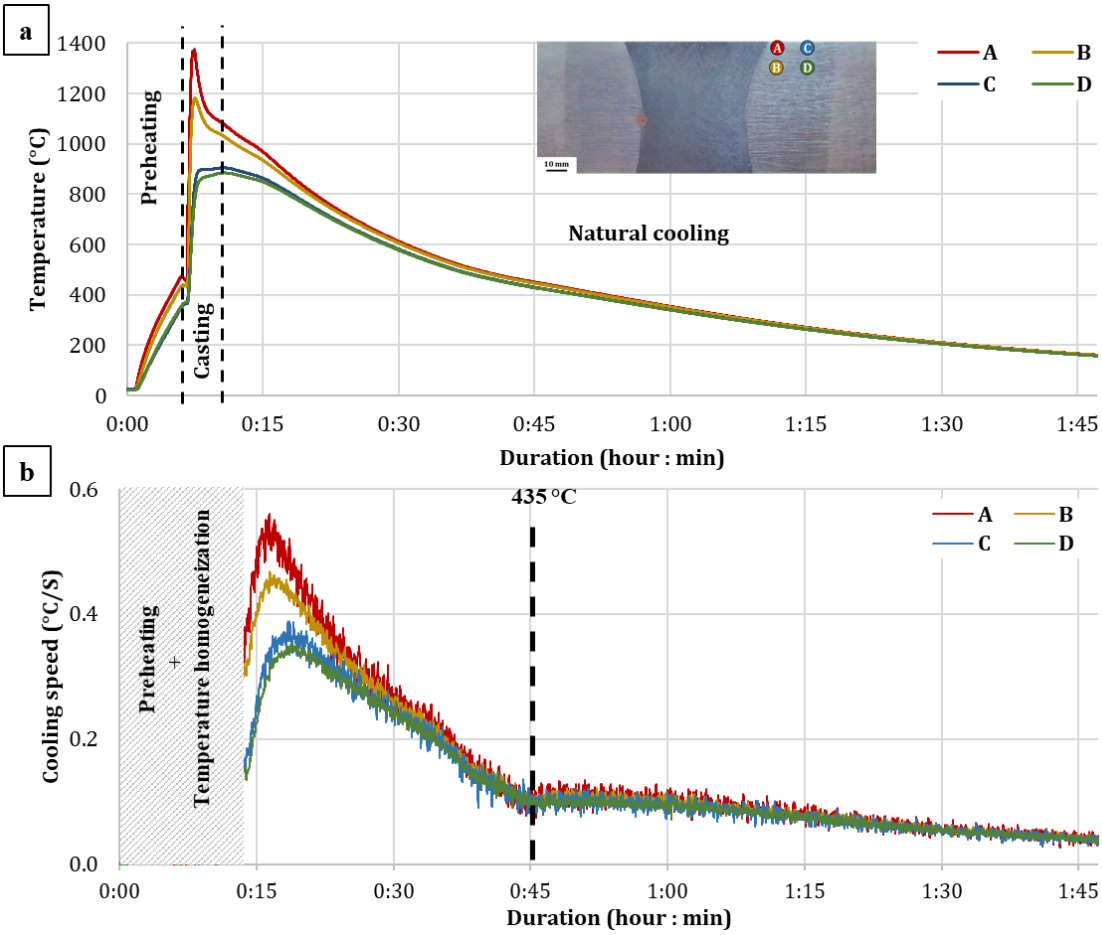

Figure 9: a- Thermal welding cycle and b- cooling speed inside the HAZ for thermocouples A (x = 33, z =1), B (x = 33, z = 10), C (x = 43, z = 1) and D (x=43, z =10). The dashed vertical line at 45 min indicates the change in slope occurring at 435°C.

Obviously, the higher the distance with the solidified zone, the lower the peak temperature. Since the width of the weld seam depends on the depth considered, peak temperature at a given x position also does. As a result, since the weld seam is wider at z = 1 mm compared to z =10 mm, peak temperature is higher in close surface compared to sub-surface. However, with increasing distance from the SZ, temperature homogenization leads to lower differences in peak temperatures. Peak temperatures at thermocouples C and D are similar (904°C and 884°C, respectively). Thus, close to the SZ, the impact of depth inside rail head is primordial but, the further away from it, the weaker is the impact.

The peak temperature of thermocouple C is 904°C, which is very close to the position of Ac3, whose temperature is 877°C. As a result, the position of this thermocouple is assimilated to the position where Ac3 is reached.

When investigating cooling speed evolution (Figure 9.b), a clear change in slope is detected at 435 ± 5°C. This temperature is close to Bainitic start (Bs) temperature, as provided by Saarstahl Rail (442°C, see Table 2). It is thus reasonable to consider that this change of slope corresponds to the transition from a fully austenitic microstructure to a mixed microstructure of bainite and retained austenite at this temperature.

3.2.2. Extension of thermal history to other areas of HAZ

The welding process has then been modelled *via* a homemade Python code. The main objective of this modelling is to extend the experimental data obtained by thermocouples to a wider range of distances from the SZ. The thermal history simulated, and especially maximum temperature reached in a given position, will be linked with the resulting microstructure determined experimentally. Austenite decomposition mechanisms proposed in the literature for tempering process, are then confronted with the microstructures and thermal histories investigated in this work.

Each experimental welding step indicated in Figure 4 has been strictly modelled.

The model leans on heat transfer equation using finite element method, following equation 2 [59].

$$\delta T_t(x,z) = \alpha * \delta t * \left(\frac{\delta T_t(x,z)}{\delta x} + \frac{\delta T_t(x,z)}{\delta z}\right) \quad (2)$$

with $T_t(x,z)$ being the temperature for a given time *t*, position *x* and depth *z*, α being the thermal diffusivity of CFB steel, δx and δz being the spatial interval, both fixed at 1 mm and δt the temporal interval. α is calculated as (equation 3):

$$\alpha = \frac{k}{\rho C_p} \quad (3)$$

With *k* the thermal conductivity, estimated using Wiedemann-Franz-Lorentz law [60], ρ the density considered constant at 7.87 g/cm^3 [61] and *Cp* the heat capacity. The impact of microstructure, and especially the modification α during austenite to bainite transformation, is neglected. Natural cooling is assumed to follow Newton's cooling law (equation 4):

$$\delta T_t(x=0,z) = h(x,t) * \frac{T_t(x=0,z) - T_{air}}{dt} \quad (4)$$

with T_{air} assumed constant and fixed at 25°C and $h(x,t)$ being the thermal exchange coefficient, defined as (equation 5 [62]):

$$h(x,t) = -\frac{\rho V C_P}{A*(T_t(x,z=0) - T_{air})} * \frac{dT}{dt} \quad (5)$$

with *V* being the volume of a single finite element (1 mm^3) and *A* its area (1 mm²). For simplification purpose, only natural cooling and conduction are considered. Rail thermal radiation is neglected.

The rail presents a complex 3D shape which makes the calculation costly. This work focuses on the consequence of the thermite process on the microstructure of the rail in the vicinity of its surface, where RCF defects are likely to occur. Thus, this simulation only focuses on the rail head, with no consideration of the web nor the rail foot. Thus, z is set below 50 mm (depth of the rail head) in the whole calculations.

A 2D approach has been chosen to model the evolution of thermal history along the x direction. The 2D approach is a strong limitation of this model and its extension in 3D is one of the main perspectives of this work. This 2D approach limits the applicability of the model to along the middle of the running band and neglects rail profile along *y* direction. The calculations are therefore performed in the middle of the rail (y = 0 mm) to limit the impact of this rail profile neglection. The longitudinal length is relatively short (72 mm) which may not be sufficient for reaching a steady state in the middle of the rail

(y = 0 mm). This model is therefore used for estimating the thermal history along the HAZ and accounts for the whole welding phenomenon occurring along the full rail.

Figure 10 represents the macroscopic comparison of the modelled shape of the weld seam compared to the actual one.

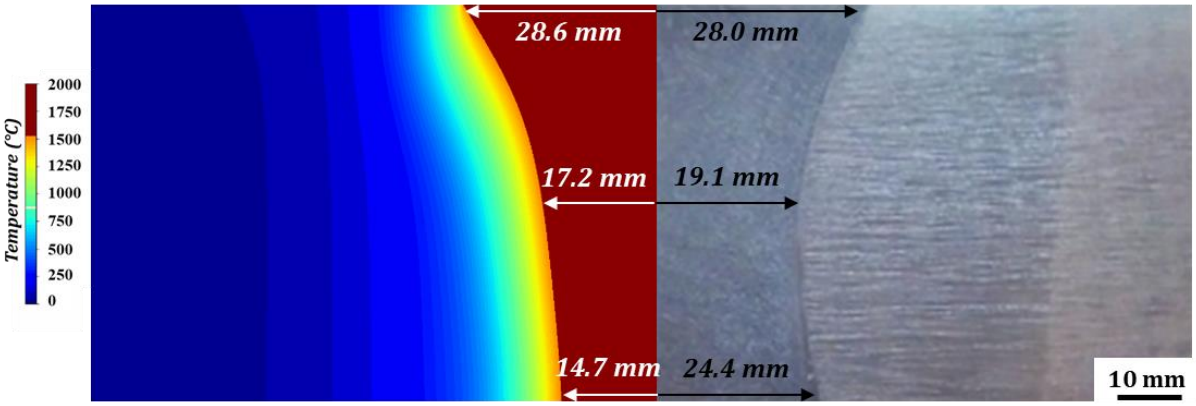

Figure 10: Comparison of the modelled temperature field at peak temperature 30 sec after thermite load inserted on the left-hand side and a transversal cut in y = 0 mm of the actual weld seam after cooling in the right-hand side.

The red color corresponds to temperatures higher than melting temperature, meaning that all red areas are liquid. The overall shape of the modelled weld seam is consistent with the actual one close to the surface but deviates when getting deeper in the rail head. This is due to the modelling of the rail head only, and not the web nor the transition zone between web and head. Heat transfer from head to web is therefore not considered, which induces significant differences in the temperature field in the lower part of the head. However, since this study focuses on the rail close surface (depths of either 1mm or 10mm), the weld seam geometry is considered consistent with the experimental one.

Resulting temperatures along the rail head at each step are shown in Figure 11. The full animation of the welding process can be found in supplementary materials.

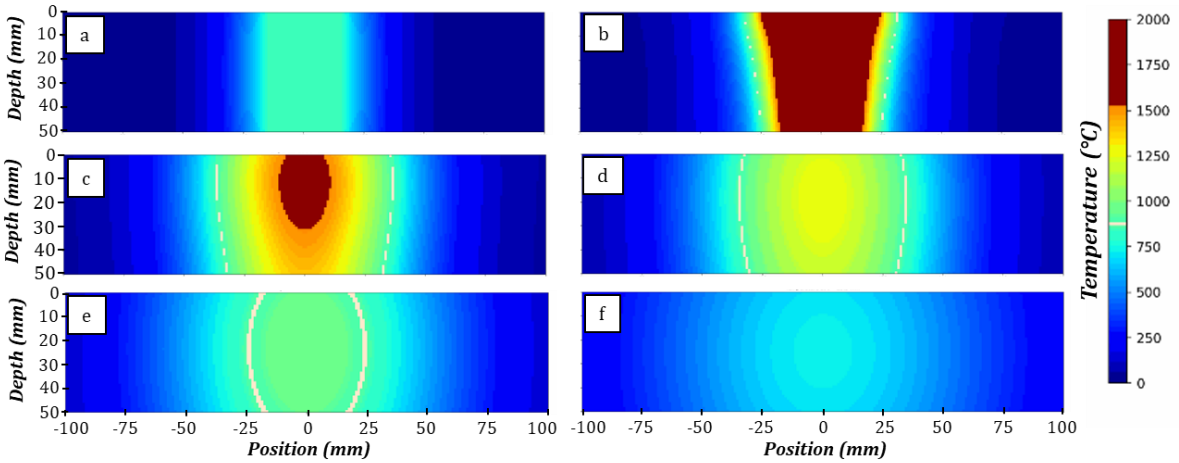

Figure 11: Simulated temperature of the rail head temperature on a transversal cut at y = 0 mm at different times: a- pre-heating (3.6 min), b- cooling with feeder after casting (7.2 min) and c-, d-, e-, f- natural cooling at respectively 12.1 min, 15.3 min, 20.8 min and 29.5 min. 877°C isothermal temperature, corresponding to BM's Ac3 temperature, is indicated in white.

The isothermal temperature of 877°C, corresponding to base material Ac3 temperature, is highlighted in white.

Resulting from this simulation, local thermal history can be extracted. Figure 12 plots the thermal histories recorded by thermocouples compared to those simulated at the same distance away from the fusion line of the solidified zone. For a better readability of the figure, only thermocouples B and D are indicated.

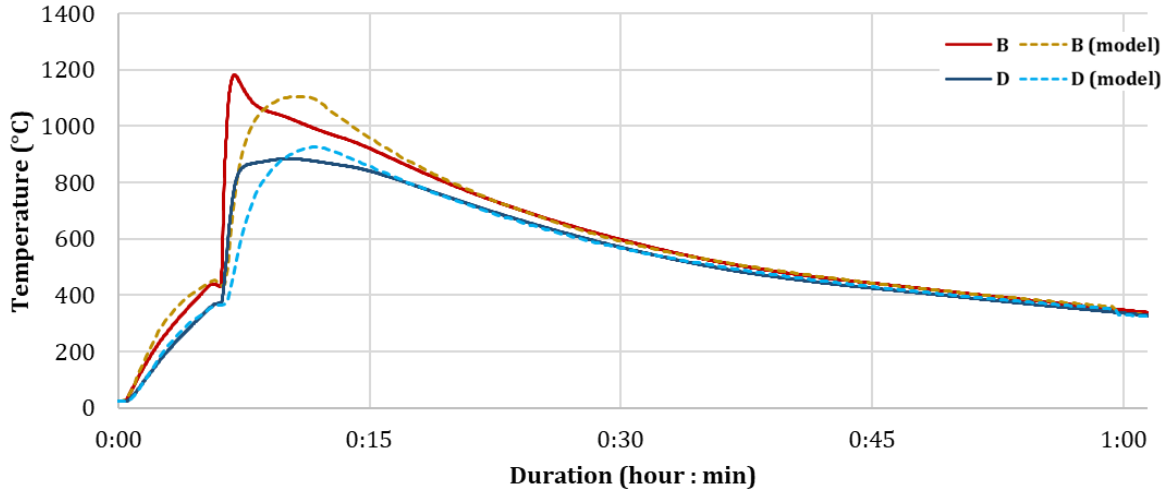

Figure 12: Comparison of experimental and simulated thermal cycles at two positions in the HAZ: at thermocouples B and D.

Figure 12 indicates that the overall simulation is consistent with the experiment, while some discrepancies remain. The preheating (0-6 min) and natural cooling parts (9-60 min) are consistent and representative of the experimental data. Some variations between experimental and simulated data are observed during casting, especially immediately after casting the portion. The use of 2D approach implies the neglection of the influence of the feeder on the side of the rail (Figure 4.c and d), which significantly affects cooling when sand mold is present. This induces some discrepancies in the calculations after portion casting prior to vent risers removal. Once vent risers are removed (3 min after the casting), the discrepancies become significantly lower. This might also be partly due to thermocouple heating rate during experimental measurement, leading to an artificial increase of temperature measured at the early stage of casting. Nonetheless, the overall simulated results are mostly consistent with experimental data.

To further confirm the validity of the simulation, it is confronted to experimental observations performed during etching. As indicated on prior Figure 5, a greenish area is observed after etching at 25 mm from the SZ, which has been attributed to a maximal temperature reached equal to Ac1 (745°C) thanks to hardness profile. Thus, thermal history has been simulated at 25 mm from the SZ, expecting a maximal temperature of 745°C. Resulting simulation (Figure 13) indicates a maximal temperature of 755°C, which is close to the expected result. The simulation is thus considered as reliable despite its

initial assumptions. An error of about 20°C, originating mainly from the geometrical variation around the position of each sub-region, is considered for the calculated temperatures.

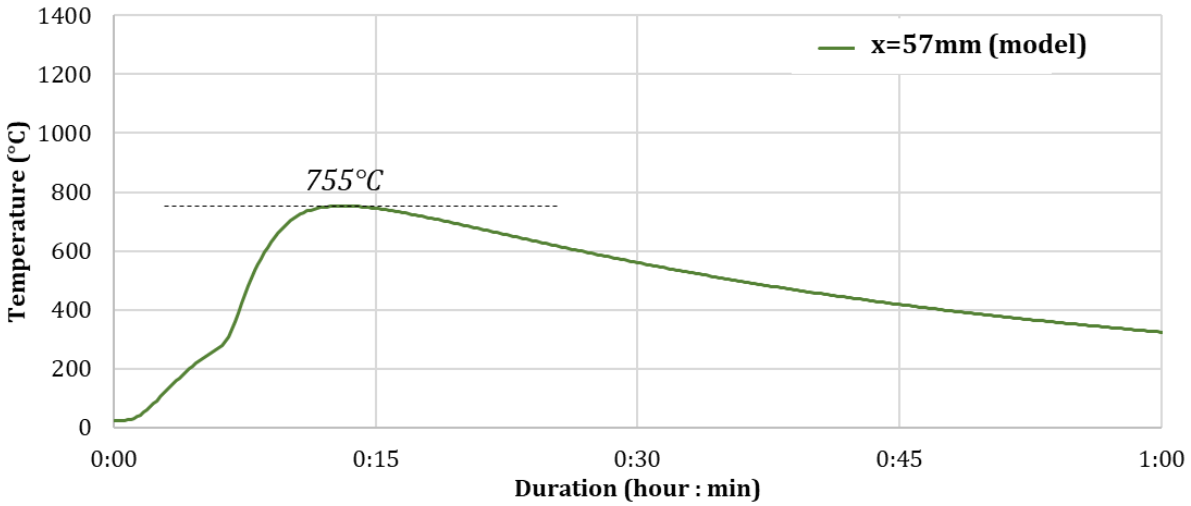

Figure 13: Simulated thermal cycle at x=57 mm, where maximum temperature is experimentally believed to be close to Ac1 (745°C)

As seen on Figure 13, the maximal temperature is reached during a plateau, which induces a prolongated exposition close to this temperature. In the case of Figure 13, for example, the rail is exposed to temperature comprised between 725°C and 755°C for more than 6 minutes. Moreover, due to temperature homogenization inside the rail, temperatures between 200°C and 300°C are held for more than 20 min in most of the HAZ, which is similar to a tempering process.

Using this simulation, the position of each observed accident on hardness profile is linked to an estimated temperature. Combining these estimated temperatures with hardness profile, the aforementioned IC and SC regions can be refined. In both regions, two distinct sub-regions can be observed, which are called High Temperature (HT) and Low Temperature (LT), respectively. Between these two regions, a hardness plateau is observed inside SC region. The region which experienced a temperature lower than Ac1 (temperatures slightly lower than Ac1) is denoted SC-Ac1. The transition zone (Transi BM) denotes the region where maximum temperature reached is low (< 390°C), while significantly different from BM in terms of phase content and hardness.

These regions and sub-regions, as well as corresponding temperatures, are indicated in Figure 14. Peak temperature is extracted from simulation for each x values of the borders of each zone along x direction.

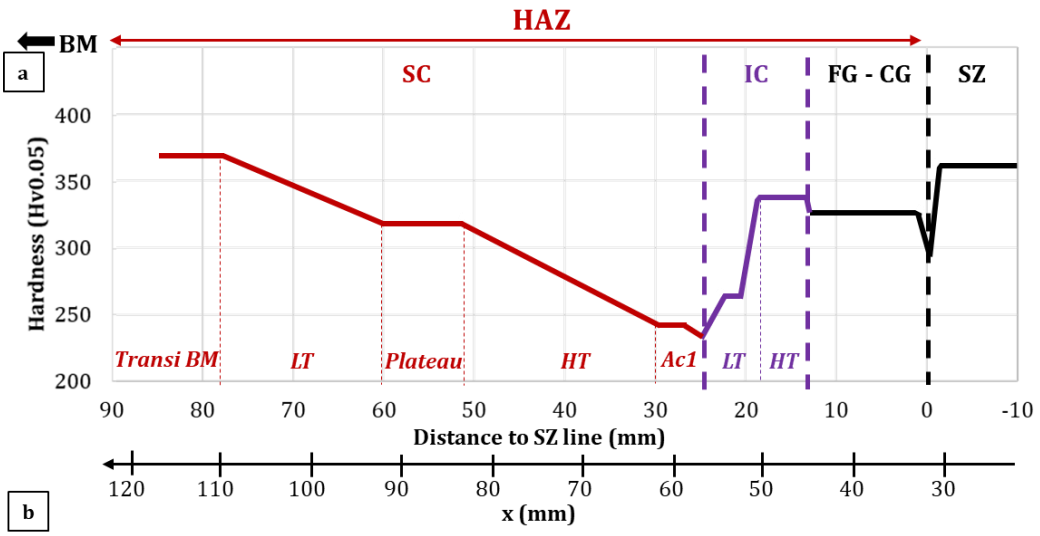

Zone	Position interval x (mm)	Calculated peak temperature
SZ	0 – 32	$T_{max} > MT$
CG	32 – 34	$MT > T_{max} \sim T_{solidus}$
FG	34 – 46	$T_{solidus} > T_{max} > Ac3$
IC – HT	46 – 50	$820°C < T_{max} < Ac3$
IC – LT	50 – 55	$Ac1 < T_{max} < 820°C$
SC – Ac1	55 – 62	$T_{max} \sim Ac1 - \delta T$
SC – HT	62 – 83	$520°C < T_{max} < Ac1$
SC – Plateau	82 – 92	$460°C < T_{max} < 520°C$
SC – LT	92 – 112	$390°C < T_{max} < 460°C$
SC – Transi BM	112 – BM	$T_{max} < 390°C$
BM	-	$T_{max} \sim$ ambient

Figure 14: a- Scheme of the hardness profile inside HAZ and corresponding regions and sub-regions. b- calculated temperature range of each sub-region, taken as the temperature at each x values of the borders of each zone along x direction

Obviously, the regions with the lowest hardness, namely SC-HT and SC-Ac1 are weak spots for further rail solicitation, more sensitive to stress concentration. Investigations of a worn rail of similar chemical composition confirms that all RCF cracks occur at the same position, between 2 cm and 3 cm from the solidified zone; most of them being located at slightly more than 2 cm from the SZ [21], which corresponds to the start of the SC region. A focus on these sub-regions will therefore be made during this work. However, for comprehensive purpose, attention will be paid to the rest of SC and IC regions. The microstructure and hardness of FG and CG regions are not presented herein.

3.3. Microstructure along Heat Affected Zone

The microstructures in each sub-region of the IC and SC zones are carefully investigated to understand the reasons beneath observed hardness loss. For comprehensive purpose, the microstructure evolution is presented from the region further away from the weld, starting from SC-LT, to the hottest region, up to Ac3 temperature (IC-HT). All investigations are performed in the middle of each sub-

region, except for SC-Ac1 and IC-LT, where investigations are located immediately around Ac1 isotherm (left-hand side and right-hand side, respectively). To feature close surface information, all the investigations are performed at z = 1 mm. Due to temperature homogenization, as discussed in section 3.2.1, the peak temperature and overall thermal history are similar in surface and with depth for the areas of interest (SC to IC) inside rail head. Thus, the microstructures at 1 mm depth are considered representative to the microstructures in sub-surface.

Figure 15 indicates the band contrast and phase map of each sub-region. The microstructure of the base material, indicated in prior Figure 2, is added to this figure for comparative purpose.

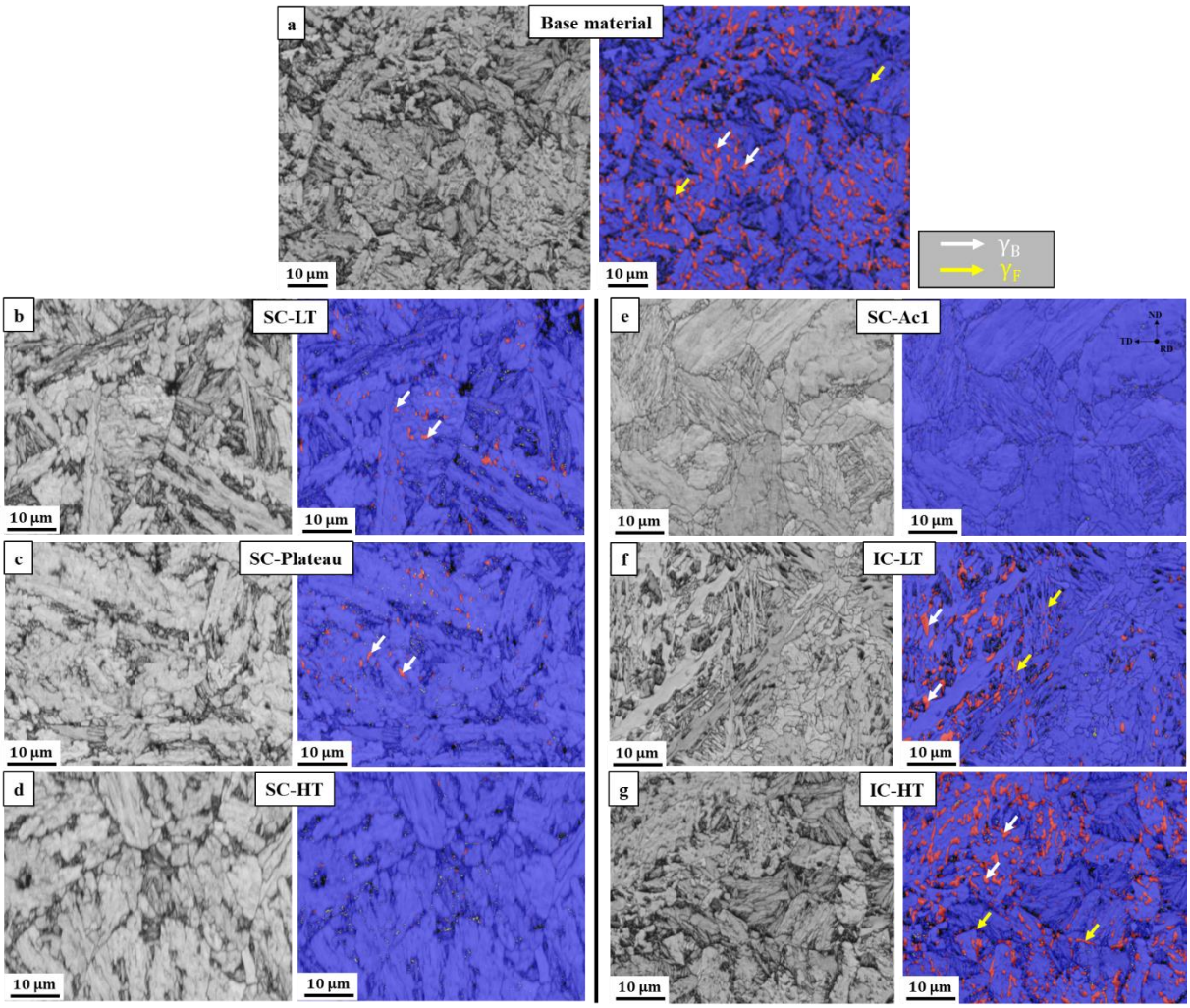

Figure 15:Band contrast and phase maps of each sub-region along the HAZ at a 1 mm depth from the top surface. Bainitic ferrite is indicated in blue in phase maps while austenite is in red. Arrows in white and yellow have been added to highlight γ_B and γ_F, respectively. a- Base Material (reminder from Figure 2, please refer to this figure for a better resolution), b-SC-LT, c- SC-Plateau, d- SC-HT, e-SC-Ac1, f- IC-LT, g- IC-HT

As stated earlier (section 3.2.1), no austenite is found in SC-Ac1 sub-zone while a significant amount of austenite is noticed a few dozen micrometers closer from the weld seam (IC-LT). This corresponds to Ac1 temperature and perfectly match the position of the greenish area observed after etching.

Figure 16 synthetizes the phase content evolution related to the hardness evolution of each of these sub-regions. The presence of carbide phase is only qualitatively indicated since the dimensions of most carbides are too small to be indexed by EBSD. TEM investigations enable the observation of lower scale particles, but the statistical representativeness of such analysis is too shallow to ensure a satisfactory quantification.

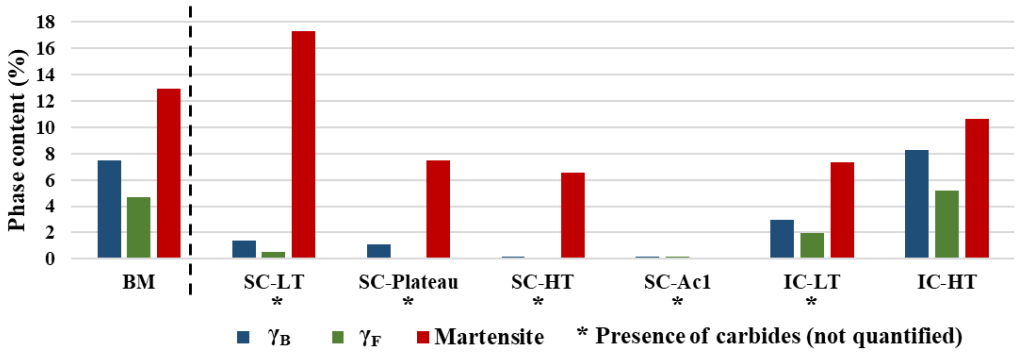

*Figure 16:Surfacic phase content measured by EBSD and XRD in each sub-region of the HAZ as well as in base material for comparative purpose. The existence of carbides is indicated by a * symbol but could not be quantified.*

Close to BM, one can notice the trend of martensite increase and austenite reduction. With increasing temperatures, both austenite and martensite content are then rapidly lowered, until complete depletion of both phases at SC-Ac1. Once reaching maximum temperatures higher than Ac1, in IC region, reaustenitization occurs and phase content and hardness get gradually closer to base material ones. Since the TRIP effect is the main factor impacting RCF resistance, the disappearance of austenite inside SC-HT and SC-Ac1 implies a minimum in RCF resistance locally. The reasons beneath phases changes are detailed hereafter.

4. Discussions

4.1. Phase content evolution along Heat Affected Zone

The parameter impacting the most significantly RCF resistance in TRIP-aided steels is austenite mechanical stability, since it governs TRIP effect. However, during welding, it is possible to transform up to all austenite prior to solicitation due to thermal history. Thus, in the HAZ, thermal stability is prevalent, and is the main consideration of this work. Numerous authors [63–65] performed tempering treatments at various temperatures to examine the transformation of austenite in a carbide-free bainite. While thermite welding is considerably more complex than controlled tempering, the resulting phase transformations have been found to be similar. Sourmail *et al.* [64] indicated that austenite can be decomposed or destabilized following mainly two mechanisms. At temperature lower than 550°C, corresponding to SC-LT region, a so-called indirect decomposition is mainly observed where tiny amounts of cementite precipitate inside austenite [64,66–68]. Resulting transformation depletes the remaining austenite from carbon, hereby destabilizing it [66,69–71]. During cooling at room temperature, this austenite eventually transforms into martensite [66,69,70]. This can easily be seen in

SC-LT region (maximum calculated temperature lower than $460_{\pm 20}$°C), where a significant increase of martensite is observed (Figure 16), going with the formation of numerous tiny carbides (Figure 17).

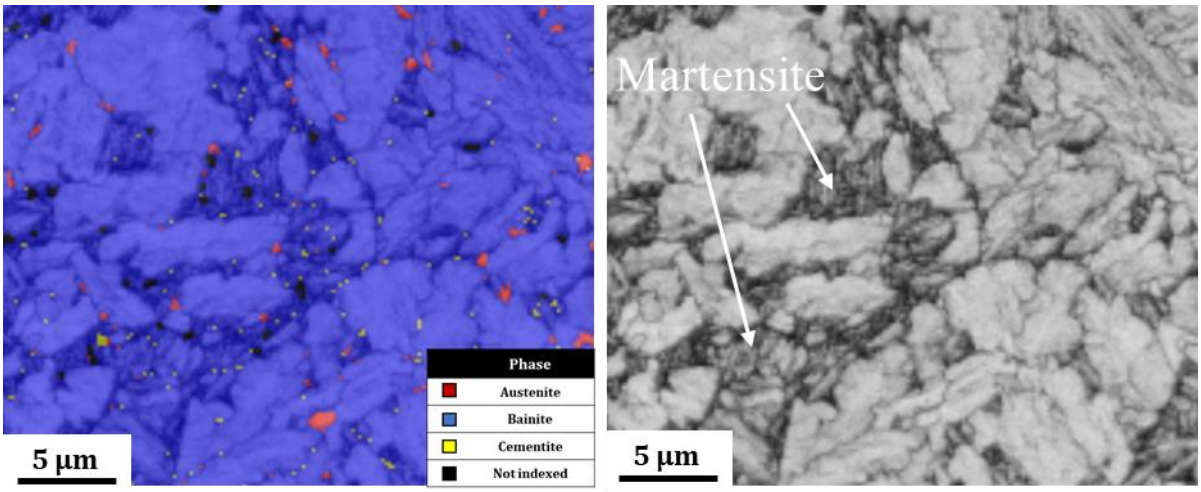

Figure 17: Phase map overlapped with band contrast as well as band contrast of SC-LT region, indicating the formation of tiny carbides as well as martensite.

For higher temperature, but lower than Ac1 (500°C - 700°C), a so-called direct decomposition is observed. Austenite transforms into discrete particles of cementite in a ferritic matrix [64,66–68]. This is typically observed inside SC-Ac1 and SC-HT (520 $_{\pm 20}$°C to 745 $_{\pm 20}$°C calculated), where austenite films are partly transformed into fine interlath carbides (Figure 18).

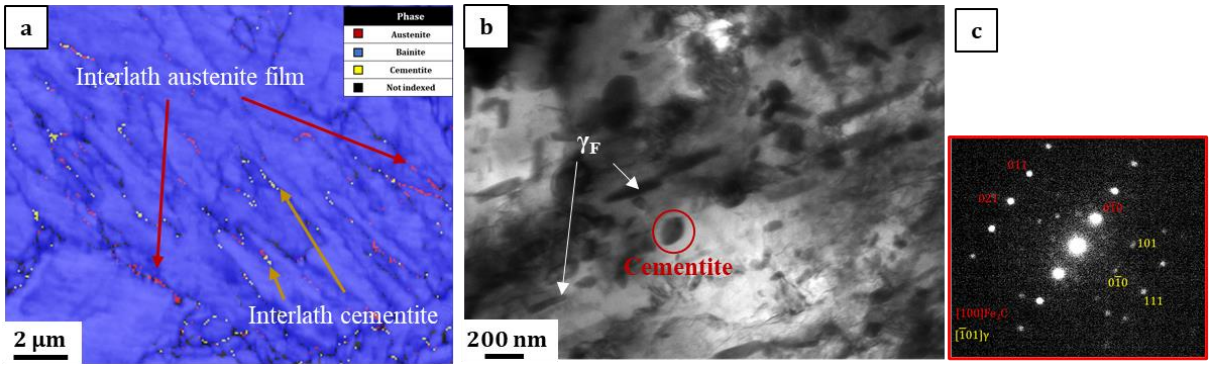

Figure 18: Microstructure of SC-Ac1 sub-region. Untransformed austenitic films coming along cementite observed between bainitic laths, as indicated by a- EBSD phase map and b- c-cementite particle observed by TEM and c- corresponding SADP, cementite being the second phase that grew upon an austenitic matrix

At intermediate temperatures, corresponding to SC-Plateau ($460_{\pm 20}$°C - $520_{\pm 20}$°C) both martensite and cementite particles are evidenced experimentally (Figure 16). The co-existence of carbides and martensite in SC-Plateau region is likely to be a consequence of the co-occurrence of direct and indirect transformation at these temperatures, which is in good adequation with the temperature range where direct and indirect decompositions co-exist [64]. Austenite blocks are partly transformed into cementite (Figure 19), while almost all austenite films are already almost fully transformed.

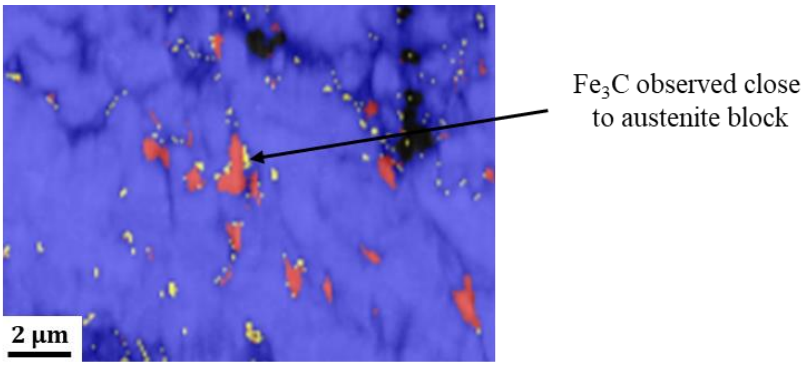

Figure 19: Phase map of SC-Plateau sub-region. Carbides are clearly observed along the grain boundaries and in proximity of austenitic blocks. Blue indicates bainitic ferrite and martensite (darker areas), red indicates austenite (γ_B or γ_F) and yellow indicates carbides.

At temperatures higher than Ac1 position, in IC-LT region, a heterogeneous microstructure is observed, possibly due to local carbon migration. Figure 20.a presents a mostly ferritic structure with coarse Fe_3C (up to a few micrometers wide). In Figure 20.b, numerous austenitic grains of several micrometers are observed alongside carbides. Austenitic films, which are usually smaller than 1 µm length and have a few hundred nanometers width in the base material, are here of the order of a few micrometers. Both Figure 20.a and Figure 20.b are observed at less than 50 µm from each other.

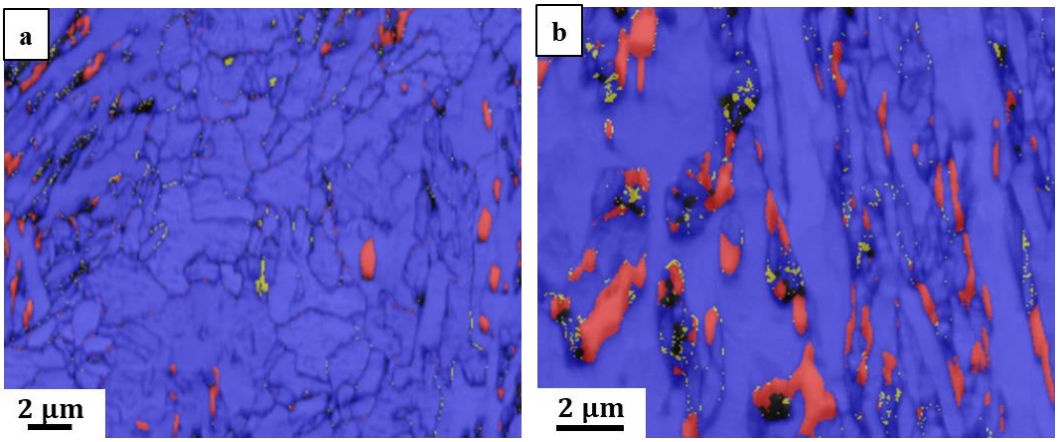

Figure 20: Microstructure heterogeneities inside IC-LT. Both zones are indexed at less than 50 µm from each other. a- phase map representing a mostly ferritic matrix with high dimension Fe_3C particles. b- phase map representing a former CFB matrix with austenite decomposition into Fe_3C particles.

For increasing temperatures starting from this point, the microstructure becomes gradually closer to initial microstructure. Finally, when reaching IC-HT region, a microstructure mostly similar to the BM is observed, with the noticeable exception of a small increase of γ_F and blocks content and dimensions compared to BM (Figure 21). The microstructure is however heterogeneous, with austenite depleted areas along with austenite rich areas. These microstructural heterogeneities may arise from carbon distribution heterogeneity from one grain to another. Very few cementite is noticed in this region.

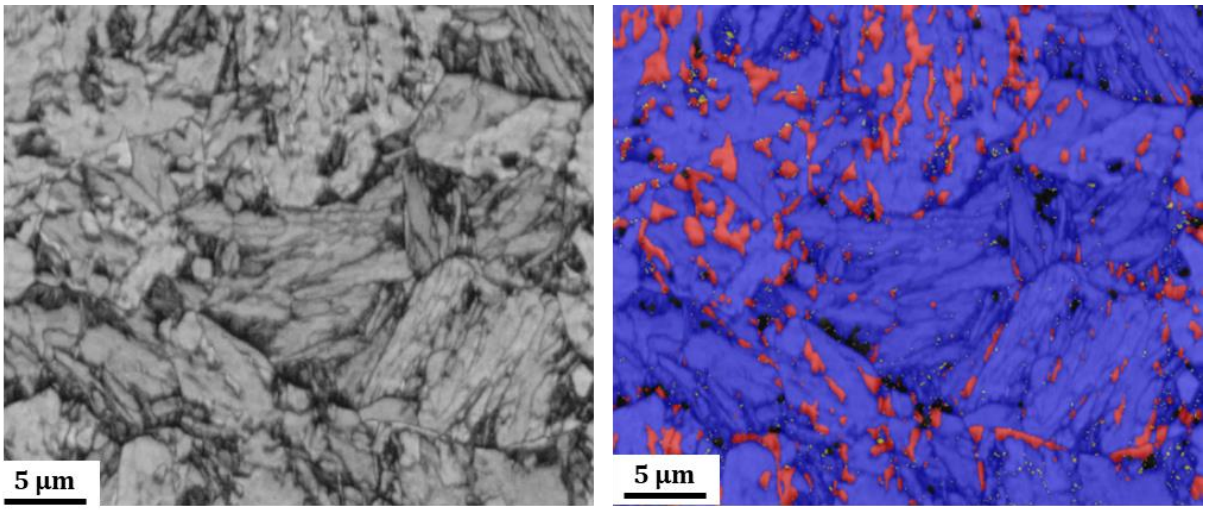

Figure 21: Band contrast and phase maps of IC-HT at 1 mm from the top surface. Bainitic ferrite is indicated in blue in phase maps while austenite is colored in red.

Figure 22 synthetizes these transformations and resulting phase content compared to base material's, linking the temperature to the rail position. Seeing the thermal history indicated in Figure 12, for the region experiencing direct decomposition, indirect decompositions is also likely to occur. Indeed, during cooling, this region is kept at temperatures ranging from 400°C to 500°C for more around 14 minutes, which will induce indirect decomposition additionally to direct decomposition.

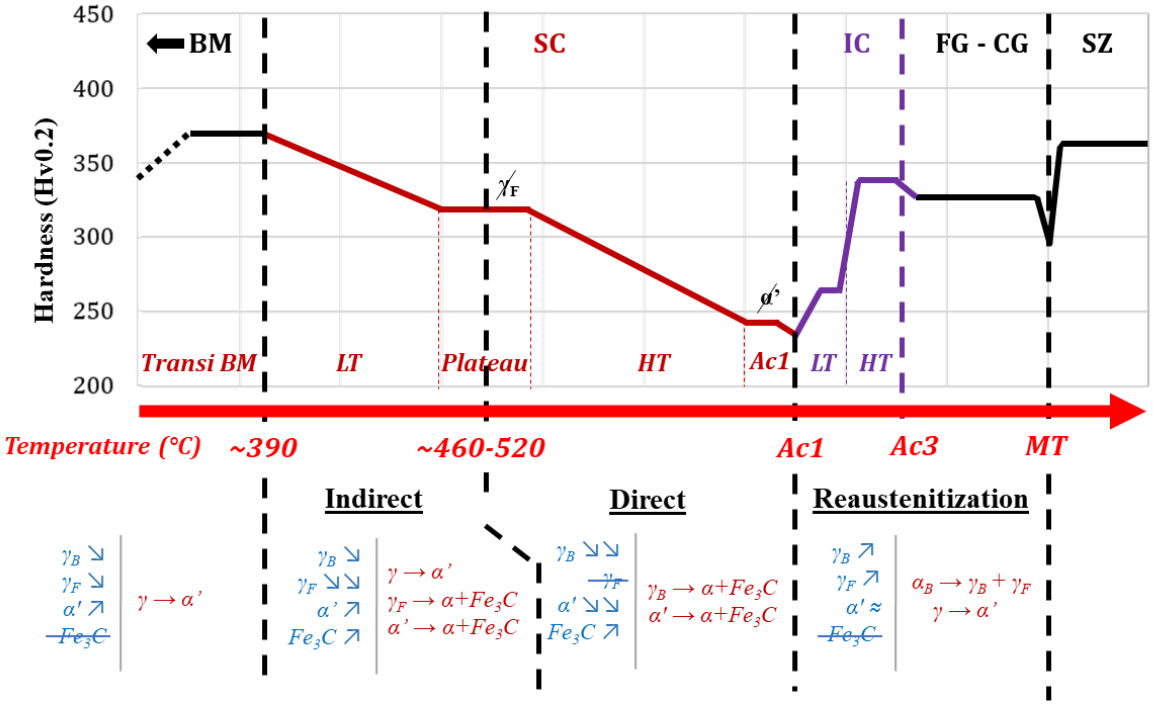

Figure 22: Hardness evolution along the HAZ, linked with the main phase transformations observed depending on the maximum temperature reached. Text in blue indicates the evolution of each phase content compared to BM while text in red indicates the main transformations observed in this area.
γ = austenite, α = ferrite, α' = martensite, $α_B$ = bainitic ferrite, MT = melting temperature

4.2. Austenite block vs. austenite film thermal stability

Thermal history during welding is partly responsible for austenitic phase chemical composition and potential phase transformation. However, temperature itself is not the only factor explaining the previously discussed phase transformations. Indeed, for a given temperature, each phase has its own thermal stability, depending on numerous parameters, listed for example by Wang *et al.* [63], including local chemical composition, austenite size, morphology, crystallographic orientation compared to rolling direction, surrounding matrix and micro-stress/strain distribution. One of the main parameters impacting thermal stability of retained austenite is related to its chemical composition. This is mainly addressed by the content of gamma favoring elements, and especially carbon content [72], which is, in turn, mostly dependent on austenite shape [48,49,52].

To understand the differences between γ_B and γ_F during steel tempering, local chemical composition has been investigated *via* Atom Probe Tomography (APT) inside each phase (Figure 23). These investigations were performed inside the base material to determine the initial configuration of austenite, prior to the welding process.

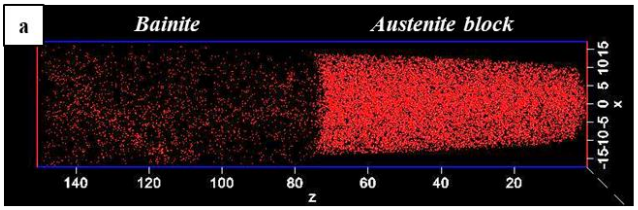

b Phase		Bainite	Martensite	γ_B	γ_F
Composition (at%)	C	0.1 *< 0.1*	0.3 *±0.2*	4.4 *±0.7*	6.5 *±0.6*
	Cr	0.5 *±0.1*	0.5 *±0.1*	0.6 *±0.1*	0.6 *±0.1*
	Si	2.6 *< 0.1*	2.9 *±0.3*	3.1 *±0.3*	2.8 *±0.2*
	Mn	1.2 *±0.2*	1.3 *±0.2*	1.6 *±0.2*	1.5 *±0.2*
	Fe	Bal.	Bal.	Bal.	Bal.

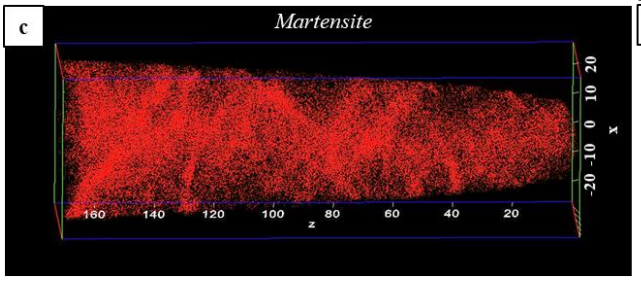

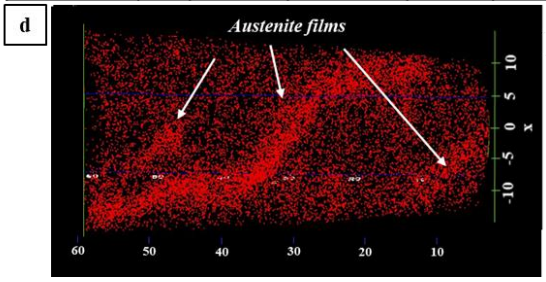

Figure 23: Chemical composition investigations performed via Atom Probe Tomography, indicating the carbon distribution in different phases, namely a- bainite and γ_B, c- martensite and d- austenite film surrounded by bainite. Sub-figure b- indicates the average chemical composition of each phase and its standard deviation, in atomic percent.

Chemical composition, and especially carbon content varies significantly depending on the considered phase. Carbon distribution is relatively homogeneous in bainite and in austenite whatever its shape (Figure 23). While bainite is almost carbon depleted due to its low solubility (slightly higher than 0.1 at% [73,74]) in this phase [75,76], a much higher content of carbon is observed inside austenite, up to 6.5 at% inside γ_F and 4.4 at% inside γ_B (Figure 23.b). Inside martensite (Figure 23.c), a heterogeneous carbon distribution, with needle-like zones with excessive concentration of carbon, are observed.

Carbon content has complementary effects on the thermal stability of austenite depending on maximum temperature reached during welding. As described by Hidalgo *and al.* [77], carbon enrichment of austenite is desired to stabilize this phase upon martensitic transformation during quenching. Thermal stability at low temperature is thus increased in the absence of cementite

precipitation. However, increasing carbon content leads to an increase in the driving force for cementite precipitation increases. Thus, adversely to mechanical stability [48,78,79], in the context of thermal stability, γ_F, is less stable than γ_B [80]. In the indirect decomposition range, the early formation of tiny carbides leads to carbon depletion in its surrounding. This leads to a destabilization of austenite, which in turn transforms into secondary martensite on cooling [50,64,69]. Since this carbide precipitation is more likely for higher carbon content, γ_F is especially sensitive to this transformation. For higher temperature, austenite directly transforms into ferrite and cementite [50,64] due to carbon partitioning. This is confirmed experimentally in Figure 16.b, where γ_F is depleted at lower temperature compared to γ_B.

4.3. Rail optimization

4.3.1. Targeted optimization

As indicated in the introduction, TRIP effect is the main contributor explaining the high RCF resistance of CFB in railways applications. The positive effect of TRIP is maximized when an optimum in austenite mechanical stability is reached. If austenite mechanical stability is too low, austenite transforms early into martensite, leaving no austenite left for further solicitation. Moreover, excessive austenite transformation leads to massive amount of hard and brittle martensite, which acts as crack initiation site and must be avoided [22,81]. In the other hand, if austenitic stability is too high, there is no more possibility for TRIP effect to occur [16,82]. γ_B is less mechanically stable and transformed prematurely, while γ_F is transformed under higher solicitation, hence allowing a higher rail lifetime [16,22,83]. Thus, if one considers solely base material's performances, austenite must be engineered in the shape of film, rather than block. This has already been successfully performed in the current grade *via* chemical composition and heat treatment optimization.

However, the most challenging issue with bainitic steels is that TRIP effect is not the only way to transform austenite. Thermal transformation of austenite is also observed. Thermal transformation might occur during rail service at some extent, during which local temperature may range from 650°C [84,85] to 1300°C [86–88]. However, the duration of heating is low, and only 0.8 ms is needed for a complete heating and cooling cycle (down to 46°C) after a single wheel pass [89]. Moreover, this thermal cycle is only localized to the first few micrometers under the surface, which limits its impact on the overall performance, especially since wear resistance is low. During welding, however, this heating contribution becomes prevalent since temperatures higher than Ac3 are reached for several minutes and up to three hours are needed for a complete cooling down to room temperature of the rail. As a result, during the welding process, some austenite transforms, depending on its position inside the HAZ [90]. Since this transformation occurs prior to rail service, it means that, if thermal stability of austenite is too low, no more austenite is available for TRIP effect. The beneficial contribution of TRIP is therefore lowered, if not suppressed, leading to a noticeable decrease of RCF resistance. Thus, the optimization of austenite stability must be divided into thermal stability and mechanical stability. Thermal stability

is to be kept as high as possible, while mechanical stability, is to be optimized to obtain a prolongated TRIP effect [91,92]. The current mechanical stability of tested rail is optimized for service solicitation, with γ_F carrying most of the TRIP effect due to its high mechanical stability. However, its thermal stability is not sufficient to fully withstand the welding process. As a result, the most efficient way to further improve rail's lifetime is to limit austenite transformation during the welding process. Working on γ_B/γ_F content and ratio is not effective when looking at weldability since both γ_B and γ_F are transformed during this process. Rather than modifying these ratios and contents, it would be more efficient to change the γ_B and/or γ_F intrinsic thermal stability. As discussed by Wang *et al.* [63], this is feasible through intrinsic modification of austenite, such as austenite size, morphology, crystallographic orientation, chemical composition or environmental modifications, such as surrounding matrix strength, micro-stress/strain distribution. While the existence of a temperature range where austenite is almost fully transformed seems unavoidable, its range in terms of geometrical dimensions inside the welded rail can be narrowed, thus limiting its impact on RCF resistance. While modifying the welding parameters could have some positive effects, it would hardly fully compensate the low austenitic thermal stability. Thus, the most effective way to improve rail's performances is to tune austenitic thermal stability, without degrading its mechanical stability for future RCF application.

4.3.2. Optimization strategies

To modify the intrinsic austenite thermal stability, several approaches are possible and are presented as perspectives for future work.

The first approach would be to modify the initial rail's heat treatment, prior to welding. One of the most promising thermal treatment is proposed by Bhadeshia *et al.* [50] and Wang *et al.* [93]. The authors use a two-step heat treatment in which isothermal transformation occurs at a high temperature (higher than Ms), leading to high transformation kinetics, then followed by transformation at a lower temperature (lower than Ms) where the blocks of austenite are refined. In such a treatment, the austenite stability can then be engineered so that it transforms into low dimension carbide-free bainite continuously over a large range of strain during deformation. This approach mainly leads to a refinement of both γ_F and γ_B, hereby stabilizing it [50].

The second approach would be engineering rail's chemical composition. It would enable both a modification of austenitic intrinsic stability and of its environment. While there is no guarantee that changing chemical composition would reverberate directly in austenite's local chemical composition, it would necessarily impact austenite's environment. Thus, by stabilizing CFB microstructure and avoiding its transformation into upper bainite and ferrite, a shielding effect [63] would be added, which would preserve some austenite after welding. This CFB phase stabilization could be realized through several means, but any addition of carbide retardant (Al, Si…) should be effective in stabilizing CFB. Conversely, adding strengthening elements inside the matrix leading to the precipitation of submicrometric carbides inside the matrix may guarantee a relatively high and homogeneous hardness,

while there is a risk that these carbides grow significantly during welding and impoverish their surrounding in carbon, which would be counterproductive.

5. *Conclusions*

The consequences of thermite welding on the microstructure and hardness profile of the HAZ have been investigated to identify the microstructural origin of RCF loss in the HAZ. To better understand the microstructural features observed along the HAZ, microstructure characterization has been supplemented by thermal history analysis. Thermal history inside the HAZ has been measured experimentally in specific positions *via* thermocouples insertion and extended to other positions *via* 2D modelling of the welding process. This modelling allowed to estimate the temperature range of each previously defined subregions. Moreover, the knowledge of local thermal history enabled to better understand microstructural evolution towards HAZ regions, especially towards austenite decomposition. The main results obtained are summarized below:

- Several zones have been identified inside the HAZ, each zone presenting distinct criticality towards weldability. The most critical areas towards RCF resistance and weldability are called SC-Ac1 and SC-HT in this work, corresponding to peak temperatures slightly lower than Ac1. In these areas, hardness collapses to less than 240 Hv, and almost no austenite remains. The CFB microstructure has been partly transformed into ferrite and carbides. Stress concentration is likely to occur at this position, which might induce RCF defects or failure.
- This criticality has been linked to austenite thermal stability. Austenite decomposition due to thermal input is attributed to indirect decomposition at low temperature ($T < 520°C$). Tiny amount of cementite precipitate inside austenite, destabilizing it. During cooling, austenite transforms into martensite (SC-LT and SC-Plateau regions). For temperatures higher than 460°C, direct decomposition occurs, transforming austenite into ferrite and Fe_3C. For these temperatures, indirect decomposition is also believed to occur during subsequent rail cooling.
- Adversely to mechanical stability, austenite films γ_F are less thermally stable than austenite blocks γ_B. γ_F being the main contributor to RCF resistance in base material [21], its transformation is therefore critical for future wheel/rail contacts.
- The low thermal stability of γ_F is the main weakness identified for this CFB grade. Thus, to improve rail's lifetime, increasing austenite thermal stability without degrading its mechanical stability is believed to be the most effective way. This can be achieved through modification of rail's chemical composition or by tuning rail production's thermal history, prior to welding. Chemical composition modification could be performed targeting a stabilization of the CFB microstructure, which should shield the remaining austenite, or adding carbide retardants inside the solid solution. The most promising way to improve rail's performances by thermal approach is proposed by Bhadeshia *et al.* [50]. It consists in a two steps heat treatment in which isothermal transformation occurs at temperature higher than Ms, followed by a low temperature tempering.

While this work led to the proposal of ways to increase austenitic thermal stability, these propositions could not be tested in practical applications. Perspectives of this work would first be to extend modeling to 3D, to better estimate the thermal field inside HAZ. Then, several means of increasing austenitic thermal stability should be studied. These modified grades' resistance to welding could be at first tested by realizing tempering treatments at temperatures ranging from 500°C to Ac1. The hardness and phase content investigations of such treated samples would give hints on the weldability of such improved rails.

6. Acknowledgments

This project has received funding from the Shift2Rail Joint Undertaking (JU) under grant agreement No 101012456. The JU receives support from the European Union's Horizon 2020 research and innovation program and the Shift2Rail JU members other than the Union. The authors would like to thank the French national project METSA for providing them with access to the Atom Probe Tomography platform of GPM Rouen. The APT work was carried out under the GENESIS experimental platform. GENESIS is supported by the Région Haute-Normandie, the Métropole Rouen Normandie, the CNRS via LABEX EMC, and the French National Research Agency as a part of the program "Investissements d'avenir" with the reference ANR-11-EQPX-0020.

The authors also thank Pandrol (Raimes, France), and especially A. Kanjer, for the thermit welding, thermocouple instrumentation and discussions, as well as the SEM and TEM national facilities in Lille (France), supported by the Conseil Régional du Nord-Pas de Calais, the European Regional Development Fund (ERDF), and the Institut National des Sciences de l'Univers (INSU, CNRS).

7. Data availability

The raw/processed data required to reproduce these findings cannot be shared at this time due to legal or ethical reasons.

8. References

[1] A. Ekberg, E. Kabo, Fatigue of railway wheels and rails under rolling contact and thermal loading—an overview, Wear. 258 (2005) 1288–1300. https://doi.org/10.1016/j.wear.2004.03.039.

[2] Q. Li, X. Huang, W. Huang, Fatigue property and microstructure deformation behavior of multiphase microstructure in a medium-carbon bainite steel under rolling contact condition, Int. J. Fatigue. 125 (2019) 381–393. https://doi.org/10.1016/j.ijfatigue.2019.04.019.

[3] S. Hasan, Dry rolling/sliding wear behaviour of pearlitic rail and newly developed carbide-free bainitic rail steels, Wear. (2018) 9.

[4] C.C. Viáfara, M.I. Castro, J.M. Vélez, A. Toro, Unlubricated sliding wear of pearlitic and bainitic steels, Wear. 259 (2005) 405–411. https://doi.org/10.1016/j.wear.2005.02.013.

[5] R.P. Dollevoet, Design of an anti head check profile based on stress relief, University of Twentee, 2010.

[6] J.P. Liu, Y.Q. Li, Q.Y. Zhou, Y.H. Zhang, Y. Hu, L.B. Shi, W.J. Wang, F.S. Liu, S.B. Zhou, C.H. Tian, New insight into the dry rolling-sliding wear mechanism of carbide-free bainitic and pearlitic steel, Wear. 432–433 (2019) 202943. https://doi.org/10.1016/j.wear.2019.202943.

[7] S.M. Hasan, M. Ghosh, D. Chakrabarti, S.B. Singh, Development of continuously cooled low-carbon, low-alloy, high strength carbide-free bainitic rail steels, Mater. Sci. Eng. A. (2019) 138590. https://doi.org/10.1016/j.msea.2019.138590.
[8] A.B. Rezende, S.T. Fonseca, F.M. Fernandes, R.S. Miranda, F.A.F. Grijalba, P.F.S. Farina, P.R. Mei, Wear behavior of bainitic and pearlitic microstructures from microalloyed railway wheel steel, Wear. 456–457 (2020) 203377. https://doi.org/10.1016/j.wear.2020.203377.
[9] B. Dylewski, S. Bouvier, M. Risbet, Multiscale characterization of head check initiation on rails under rolling contact fatigue: Mechanical and microstructure analysis, Wear. 366–367 (2016) 383–391. https://doi.org/10.1016/j.wear.2016.06.019.
[10] J. Wen, J. Marteau, S. Bouvier, M. Risbet, F. Cristofari, P. Secordel, Comparison of microstructure changes induced in two pearlitic rail steels subjected to a full-scale wheel/rail contact rig test, Wear. 456–457 (2020) 203354. https://doi.org/10.1016/j.wear.2020.203354.
[11] P. Jacques, Q. Furnémont, T. Pardoen, F. Delannay, On the role of martensitic transformation on damage and cracking resistance in TRIP-assisted multiphase steels, Acta Mater. 49 (2001) 139–152. https://doi.org/10.1016/S1359-6454(00)00215-9.
[12] K. Sugimoto, T. Iida, J. Sakaguchi, T. Kashima, Retained Austenite Characteristics and Tensile Properties in a TRIP Type Bainitic Sheet Steel., ISIJ Int. 40 (2000) 902–908. https://doi.org/10.2355/isijinternational.40.902.
[13] R.H. Leal, Transformation toughening of metastable austenitic steels, Thesis, Massachusetts Institute of Technology, 1984. https://dspace.mit.edu/handle/1721.1/15349 (accessed January 21, 2020).
[14] A. Kumar, A. Dutta, S.K. Makineni, M. Herbig, R.H. Petrov, J. Sietsma, In-situ observation of strain partitioning and damage development in continuously cooled carbide-free bainitic steels using micro digital image correlation, Mater. Sci. Eng. A. 757 (2019) 107–116. https://doi.org/10.1016/j.msea.2019.04.098.
[15] Z. Mei, J.W. Morris, Analysis of transformation-induced crack closure, Eng. Fract. Mech. 39 (1991) 569–573. https://doi.org/10.1016/0013-7944(91)90068-C.
[16] H.L. Yi, K.Y. Lee, H.K.D.H. Bhadeshia, Mechanical stabilisation of retained austenite in δ-TRIP steel, Mater. Sci. Eng. A. 528 (2011) 5900–5903. https://doi.org/10.1016/j.msea.2011.03.111.
[17] S.D. Antolovich, B. Singh, On the toughness increment associated with the austenite to martensite phase transformation in TRIP steels, Metall. Mater. Trans. B. 2 (1971) 2135–2141. https://doi.org/10.1007/BF02917542.
[18] R. Rementeria, L. Morales-Rivas, M. Kuntz, C. Garcia-Mateo, E. Kerscher, T. Sourmail, F.G. Caballero, On the role of microstructure in governing the fatigue behaviour of nanostructured bainitic steels, Mater. Sci. Eng. A. 630 (2015) 71–77. https://doi.org/10.1016/j.msea.2015.02.016.
[19] C. Zheng, R. Dan, F. Zhang, B. Lv, Z. Yan, J. Shan, X. Long, Effects of retained austenite and hydrogen on the rolling contact fatigue behaviours of carbide-free bainitic steel, Mater. Sci. Eng. A. 594 (2014) 364–371. https://doi.org/10.1016/j.msea.2013.11.072.
[20] A. Leiro, A. Kankanala, E. Vuorinen, B. Prakash, Tribological behaviour of carbide-free bainitic steel under dry rolling/sliding conditions, Wear. 273 (2011) 2–8. https://doi.org/10.1016/j.wear.2011.03.025.
[21] T. Lesage, M.N. Avettand-Fènoël, D. Balloy, S. Assaf, F. Cristofari, P. Secordel, Head check resistance of B320 bainitic rail steel grade, Mater. Today Commun. 31 (2022) 103259. https://doi.org/10.1016/j.mtcomm.2022.103259.
[22] Z. Dai, H. Chen, R. Ding, Q. Lu, C. Zhang, Z. Yang, S. van der Zwaag, Fundamentals and application of solid-state phase transformations for advanced high strength steels containing metastable retained austenite, Mater. Sci. Eng. R Rep. 143 (2021) 100590. https://doi.org/10.1016/j.mser.2020.100590.
[23] J.-B. Seol, D. Raabe, P.-P. Choi, Y.-R. Im, C.-G. Park, Atomic scale effects of alloying, partitioning, solute drag and austempering on the mechanical properties of high-carbon bainitic–austenitic TRIP steels, Acta Mater. 60 (2012) 6183–6199. https://doi.org/10.1016/j.actamat.2012.07.064.

[24] K. Sugimoto, M. Tsunezawa, T. Hojo, S. Ikeda, Ductility of 0.1-0.6C-1.5Si-1.5Mn Ultra High-strength TRIP-aided Sheet Steels with Bainitic Ferrite Matrix, ISIJ Int. 44 (2004) 1608–1614. https://doi.org/10.2355/isijinternational.44.1608.
[25] K.S. Choi, A. Soulami, W.N. Liu, X. Sun, M.A. Khaleel, Influence of various material design parameters on deformation behaviors of TRIP steels, Comput. Mater. Sci. 50 (2010) 720–730. https://doi.org/10.1016/j.commatsci.2010.10.002.
[26] G. Lacroix, T. Pardoen, P.J. Jacques, The fracture toughness of TRIP-assisted multiphase steels, Acta Mater. 56 (2008) 3900–3913. https://doi.org/10.1016/j.actamat.2008.04.035.
[27] K. Sugimoto, T. Hojo, J. Kobayashi, Critical assessment 29: TRIP-aided bainitic ferrite steels, Mater. Sci. Technol. 33 (2017) 2005–2009. https://doi.org/10.1080/02670836.2017.1356014.
[28] F.G. Caballero, S. Allain, J. Cornide, J.D. Puerta Velásquez, C. Garcia-Mateo, M.K. Miller, Design of cold rolled and continuous annealed carbide-free bainitic steels for automotive application, Mater. Des. 49 (2013) 667–680. https://doi.org/10.1016/j.matdes.2013.02.046.
[29] M. Soleimani, A. Kalhor, H. Mirzadeh, Transformation-induced plasticity (TRIP) in advanced steels: A review, Mater. Sci. Eng. A. 795 (2020) 140023. https://doi.org/10.1016/j.msea.2020.140023.
[30] N. Ilić, M.T. Jovanović, M. Todorović, M. Trtanj, P. Šaponjić, Microstructural and Mechanical Characterization of Postweld Heat-Treated Thermite Weld in Rails, Mater. Charact. 43 (1999) 243–250. https://doi.org/10.1016/S1044-5803(99)00006-6.
[31] H.Z. Oo, P. Muangjunburee, Improving microstructure and hardness of softening area at HAZ of thermite welding on rail running surface, Mater. Today Commun. 34 (2023) 105485. https://doi.org/10.1016/j.mtcomm.2023.105485.
[32] A. Skyttebol, B.L. Josefson, J.W. Ringsberg, Fatigue crack growth in a welded rail under the influence of residual stresses, Eng. Fract. Mech. 72 (2005) 271–285. https://doi.org/10.1016/j.engfracmech.2004.04.009.
[33] M. Messaadi, I. Grossoni, P. Shackleton, I. Shevtsov, Y. Bezin, R. Dollevoet, Rail degradation due to thermite weld discontinuities: Field experience, Eng. Fail. Anal. 128 (2021) 105585. https://doi.org/10.1016/j.engfailanal.2021.105585.
[34] Y. Chen, F.V. Lawrence, C.P.L. Barkan, J.A. Dantzig, Weld defect formation in rail thermite welds, Proc. Inst. Mech. Eng. Part F J. Rail Rapid Transit. 220 (2006) 373–384. https://doi.org/10.1243/0954409JRRT44.
[35] A. Królicka, K. Radwański, R. Kuziak, T. Zygmunt, A. Ambroziak, Microstructure-based approach to the evaluation of welded joints of bainitic rails designed for high-speed railways, J. Constr. Steel Res. 175 (2020) 106372. https://doi.org/10.1016/j.jcsr.2020.106372.
[36] C. Sonsino, Effect of residual stresses on the fatigue behaviour of welded joints depending on loading conditions and weld geometry, Int. J. Fatigue. 31 (2009) 88–101. https://doi.org/10.1016/j.ijfatigue.2008.02.015.
[37] Y. Liu, K.S. Tsang, H.J. Hoh, X. Shi, J.H.L. Pang, Structural fatigue investigation of transverse surface crack growth in rail steels and thermite welds subjected to in-plane and out-of-plane loading, Eng. Struct. 204 (2020) 110076. https://doi.org/10.1016/j.engstruct.2019.110076.
[38] A.D. Bedoya-Zapata, H. León-Henao, M. Mesaritis, L.F. Molina, M. Palacio, J.F. Santa, J.S. Rudas, A. Toro, R. Lewis, White Etching Layer (WEL) formation in different rail grades after grinding operations in the field, Wear. 502–503 (2022) 204371. https://doi.org/10.1016/j.wear.2022.204371.
[39] B. Younise, A. Sedmak, M. Rakin, N. Gubeljak, B. Medjo, M. Burzić, M. Zrilić, Micromechanical analysis of mechanical heterogeneity effect on the ductile tearing of weldments, Mater. Des. 37 (2012) 193–201. https://doi.org/10.1016/j.matdes.2012.01.001.
[40] L.B. Godefroid, L.P. Moreira, T.C.G. Vilela, G.L. Faria, L.C. Candido, E.S. Pinto, Effect of chemical composition and microstructure on the fatigue crack growth resistance of pearlitic steels for railroad application, Int. J. Fatigue. 120 (2019) 241–253. https://doi.org/10.1016/j.ijfatigue.2018.10.016.
[41] O. Orringer, J.M. Morris, R.K. Steele, Applied research on rail fatigue and fracture in the United States, Theor. Appl. Fract. Mech. 1 (1984) 23–49. https://doi.org/10.1016/0167-8442(84)90019-3.

[42] U. Zerbst, R. Lundén, K.-O. Edel, R.A. Smith, Introduction to the damage tolerance behaviour of railway rails – a review, Eng. Fract. Mech. 76 (2009) 2563–2601. https://doi.org/10.1016/j.engfracmech.2009.09.003.
[43] U. Zerbst, K. Mädler, H. Hintze, Fracture mechanics in railway applications—an overview, Eng. Fract. Mech. 72 (2005) 163–194. https://doi.org/10.1016/j.engfracmech.2003.11.010.
[44] Carbide-free bainite defects - private communication, (n.d.).
[45] H.K.D.H. Bhadeshia, Some phase transformations in steels, Mater. Sci. Technol. 15 (1999) 22–29. https://doi.org/10.1179/026708399773002773.
[46] F.G. Caballero, H.K.D.H. Bhadeshia, K.J.A. Mawella, D.G. Jones, P. Brown, Design of novel high strength bainitic steels: Part 1, Mater. Sci. Technol. 17 (2001) 512–516. https://doi.org/10.1179/026708301101510348.
[47] C. Garcia-Mateo, F.G. Caballero, Design of carbide-free low-temperature ultra high strength bainitic steels, Int. J. Mater. Res. 98 (2007) 137–143. https://doi.org/10.3139/146.101440.
[48] C. Hofer, H. Leitner, F. Winkelhofer, H. Clemens, S. Primig, Structural characterization of "carbide-free" bainite in a Fe–0.2C–1.5Si–2.5Mn steel, Mater. Charact. 102 (2015) 85–91. https://doi.org/10.1016/j.matchar.2015.02.020.
[49] P.V. Moghaddam, J. Hardell, E. Vuorinen, B. Prakash, The role of retained austenite in dry rolling/sliding wear of nanostructured carbide-free bainitic steels, Wear. 428–429 (2019) 193–204. https://doi.org/10.1016/j.wear.2019.03.012.
[50] H.K.D.H. Bhadeshia, Bainite in steels: theory and practice, Third edition, Maney Publishing, Leeds, UK, 2015.
[51] A.M. Gola, M. Ghadamgahi, S.W. Ooi, Microstructure evolution of carbide-free bainitic steels under abrasive wear conditions, Wear. 376–377 (2017) 975–982. https://doi.org/10.1016/j.wear.2016.12.038.
[52] B. Liu, W. Li, X. Lu, X. Jia, X. Jin, The effect of retained austenite stability on impact-abrasion wear resistance in carbide-free bainitic steels, Wear. 428–429 (2019) 127–136. https://doi.org/10.1016/j.wear.2019.02.032.
[53] S. Sekfali, Influence de la microstructure sur le comportement local dans les aciers 16MND5, PhD thesis, Ecole Centrale Paris, 2009.
[54] M. Muniz-Mangas, Welding of bainitic rail steels, University of Sheffield, 2017.
[55] K.M. De Souza, M.J.S. de Lemos, Advanced one-dimensional modeling of thermite reaction for thermal plug and abandonment of oil wells, Int. J. Heat Mass Transf. 205 (2023) 123913. https://doi.org/10.1016/j.ijheatmasstransfer.2023.123913.
[56] Y. Liu, K.S. Tsang, E. Tan Zhi'En, N. Alagu Subramaniam, J.H.L. Pang, Investigation on material characteristics and fatigue crack behavior of thermite welded rail joint, Constr. Build. Mater. 276 (2021) 122249. https://doi.org/10.1016/j.conbuildmat.2021.122249.
[57] Y. Ma, H. Chen, M.-X. Zhang, A. Addad, Y. Kong, M.B. Lezaack, W. Gan, Z. Chen, G. Ji, Break through the strength-ductility trade-off dilemma in aluminum matrix composites via precipitation-assisted interface tailoring, Acta Mater. 242 (2023) 118470. https://doi.org/10.1016/j.actamat.2022.118470.
[58] I. Pushkareva, J. Macchi, B. Shalchi-Amirkhiz, F. Fazeli, G. Geandier, F. Danoix, J.D.C. Teixeira, S.Y.P. Allain, C. Scott, A study of the carbon distribution in bainitic ferrite, Scr. Mater. 224 (2023) 115140. https://doi.org/10.1016/j.scriptamat.2022.115140.
[59] Y. Liu, K.S. Tsang, N.A. Subramaniam, J.H.L. Pang, Structural fatigue investigation of thermite welded rail joints considering weld-induced residual stress and stress relaxation by cyclic load, Eng. Struct. 235 (2021) 112033. https://doi.org/10.1016/j.engstruct.2021.112033.
[60] D. Ceotto, Thermal diffusivity, viscosity and prandtl number for molten iron and low carbon steel, High Temp. 51 (2013). https://doi.org/10.1134/S0018151X13010045.
[61] Y. Chen, F. Lawrence, C. Barkan, J. Dantzig, Heat transfer modelling of rail thermite welding, Proc. Inst. Mech. Eng. Part F-J. Rail Rapid Transit - PROC INST MECH ENG F-J RAIL R. 220 (2006) 207–217. https://doi.org/10.1243/09544097F01505.
[62] V.S. Warke, R.D. Sisson, M.M. Makhlouf, The effect of porosity on the austenite to bainite transformation in powder metallurgy steels, J. Mater. Res. 24 (2009) 3213–3219. https://doi.org/10.1557/jmr.2009.0379.

[63] K. Wang, X. Gui, B. Bai, G. Gao, Effect of tempering on the stability of retained austenite in carbide-free bainitic steel, Mater. Sci. Eng. A. 850 (2022) 143525. https://doi.org/10.1016/j.msea.2022.143525.
[64] T. Sourmail, L. Otter, S. Collin, M. Billet, A. Philippot, F. Cristofari, P. Secordel, Direct and indirect decomposition of retained austenite in continuously cooled bainitic steels: Influence of vanadium, Mater. Charact. 173 (2021) 110922. https://doi.org/10.1016/j.matchar.2021.110922.
[65] L. Morsdorf, A. Kashiwar, C. Kübel, C.C. Tasan, Carbon segregation and cementite precipitation at grain boundaries in quenched and tempered lath martensite, Mater. Sci. Eng. A. 862 (2023) 144369. https://doi.org/10.1016/j.msea.2022.144369.
[66] A. Saha Podder, H.K.D.H. Bhadeshia, Thermal stability of austenite retained in bainitic steels, Mater. Sci. Eng. A. 527 (2010) 2121–2128. https://doi.org/10.1016/j.msea.2009.11.063.
[67] V. Ruiz-Jimenez, M. Kuntz, T. Sourmail, F.G. Caballero, J.A. Jimenez, C. Garcia-Mateo, Retained Austenite Destabilization during Tempering of Low-Temperature Bainite, Appl. Sci. 10 (2020) 8901. https://doi.org/10.3390/app10248901.
[68] A. Królicka, F.G. Caballero, W. Zalecki, R. Kuziak, R. Rozmus, Controlling the Thermal Stability of a Bainitic Structure by Alloy Design and Isothermal Heat Treatment, Materials. 16 (2023) 2963. https://doi.org/10.3390/ma16082963.
[69] A.S. Podder, I. Lonardelli, A. Molinari, H.K.D.H. Bhadeshia, Thermal stability of retained austenite in bainitic steel: an in situ study, Proc. R. Soc. Math. Phys. Eng. Sci. 467 (2011) 3141–3156. https://doi.org/10.1098/rspa.2011.0212.
[70] A. Królicka, A.M. Żak, F.G. Caballero, Enhancing technological prospect of nanostructured bainitic steels by the control of thermal stability of austenite, Mater. Des. 211 (2021) 110143. https://doi.org/10.1016/j.matdes.2021.110143.
[71] D. De Knijf, R. Petrov, C. Föjer, L.A.I. Kestens, Effect of fresh martensite on the stability of retained austenite in quenching and partitioning steel, Mater. Sci. Eng. A. 615 (2014) 107–115. https://doi.org/10.1016/j.msea.2014.07.054.
[72] R.-M. Wu, W. Li, C.-L. Wang, Y. Xiao, L. Wang, X.-J. Jin, Stability of Retained Austenite Through a Combined Intercritical Annealing and Quenching and Partitioning (IAQP) Treatment, Acta Metall. Sin. Engl. Lett. 28 (2015) 386–393. https://doi.org/10.1007/s40195-015-0217-9.
[73] J.H. Jang, H.K.D.H. Bhadeshia, D.-W. Suh, Solubility of carbon in tetragonal ferrite in equilibrium with austenite, Scr. Mater. 68 (2013) 195–198. https://doi.org/10.1016/j.scriptamat.2012.10.017.
[74] F.G. Caballero, M.K. Miller, C. Garcia-Mateo, Carbon supersaturation of ferrite in a nanocrystalline bainitic steel, Acta Mater. 58 (2010) 2338–2343. https://doi.org/10.1016/j.actamat.2009.12.020.
[75] R. Ranjan, S.B. Singh, Isothermal bainite transformation in low-alloy steels: Mechanism of transformation, Acta Mater. 202 (2021) 302–316. https://doi.org/10.1016/j.actamat.2020.10.048.
[76] A.M. Ravi, A. Kumar, M. Herbig, J. Sietsma, M.J. Santofimia, Impact of austenite grain boundaries and ferrite nucleation on bainite formation in steels, Acta Mater. 188 (2020) 424–434. https://doi.org/10.1016/j.actamat.2020.01.065.
[77] J. Hidalgo, K.O. Findley, M.J. Santofimia, Thermal and mechanical stability of retained austenite surrounded by martensite with different degrees of tempering, Mater. Sci. Eng. A. 690 (2017) 337–347. https://doi.org/10.1016/j.msea.2017.03.017.
[78] W. Solano-Alvarez, E.J. Pickering, H.K.D.H. Bhadeshia, Degradation of nanostructured bainitic steel under rolling contact fatigue, Mater. Sci. Eng. A. 617 (2014) 156–164. https://doi.org/10.1016/j.msea.2014.08.071.
[79] M. Franceschi, R. Bertolini, A. Fabrizi, M. Dabalà, L. Pezzato, Effect of ausforming temperature on bainite morphology in a 3.2% Si carbide-free bainitic steel, Mater. Sci. Eng. A. 864 (2023) 144553. https://doi.org/10.1016/j.msea.2022.144553.
[80] H.-S. Park, J.-B. Seol, N.-S. Lim, S.-I. Kim, C.-G. Park, Study of the decomposition behavior of retained austenite and the partitioning of alloying elements during tempering in CMnSiAl TRIP steels, Mater. Des. 82 (2015) 173–180. https://doi.org/10.1016/j.matdes.2015.05.059.
[81] C. Xie, Z. Liu, X. He, X. Wang, S. Qiao, Effect of martensite–austenite constituents on impact toughness of pre-tempered MnNiMo bainitic steel, Mater. Charact. 161 (2020) 110139. https://doi.org/10.1016/j.matchar.2020.110139.

[82] C. Hofer, F. Winkelhofer, H. Clemens, S. Primig, Morphology change of retained austenite during austempering of carbide-free bainitic steel, Mater. Sci. Eng. A. 664 (2016) 236–246. https://doi.org/10.1016/j.msea.2016.04.005.
[83] Z.N. Yang, Y.L. Ji, F.C. Zhang, M. Zhang, B. Nawaz, C.L. Zheng, Microstructural evolution and performance change of a carburized nanostructured bainitic bearing steel during rolling contact fatigue process, Mater. Sci. Eng. A. 725 (2018) 98–107. https://doi.org/10.1016/j.msea.2018.04.015.
[84] M. Ertz, K. Knothe, A comparison of analytical and numerical methods for the calculation of temperatures in wheel/rail contacts, (2002) 11.
[85] K.D. Vo, A tool to estimate the wheel/rail contact and temperature rising under dry, wet and oily conditions, in: A.K. Tieu, H.T. Zhu, P.B. Kosasih (Eds.), Rome, Italy, 2014: pp. 191–201. https://doi.org/10.2495/CR140151.
[86] A. Kumar, G. Agarwal, R. Petrov, S. Goto, J. Sietsma, M. Herbig, Microstructural evolution of white and brown etching layers in pearlitic rail steels, Acta Mater. 171 (2019) 48–64. https://doi.org/10.1016/j.actamat.2019.04.012.
[87] C. Bernsteiner, G. Müller, A. Meierhofer, K. Six, D. Künstner, P. Dietmaier, Development of white etching layers on rails: simulations and experiments, Wear. 366–367 (2016) 116–122. https://doi.org/10.1016/j.wear.2016.03.028.
[88] J. Takahashi, K. Kawakami, M. Ueda, Atom probe tomography analysis of the white etching layer in a rail track surface, Acta Mater. 58 (2010) 3602–3612. https://doi.org/10.1016/j.actamat.2010.02.030.
[89] J. Wu, R.H. Petrov, M. Naeimi, Z. Li, R. Dollevoet, J. Sietsma, Laboratory simulation of martensite formation of white etching layer in rail steel, Int. J. Fatigue. (n.d.). https://doi.org/10.1016/j.ijfatigue.2016.05.016.
[90] C.N. Hulme-Smith, I. Lonardelli, M.J. Peet, A.C. Dippel, H.K.D.H. Bhadeshia, Enhanced thermal stability in nanostructured bainitic steel, Scr. Mater. 69 (2013) 191–194. https://doi.org/10.1016/j.scriptamat.2013.03.029.
[91] A. Varshney, K. Mondal, S. Sangal, Cold work induced stability of retained austenite at elevated temperature in a medium carbon high silicon steel, Mater. Sci. Eng. A. 832 (2022) 142455. https://doi.org/10.1016/j.msea.2021.142455.
[92] B. He, On the Factors Governing Austenite Stability: Intrinsic versus Extrinsic, Materials. 13 (2020) 3440. https://doi.org/10.3390/ma13153440.
[93] X.L. Wang, K.M. Wu, F. Hu, L. Yu, X.L. Wan, Multi-step isothermal bainitic transformation in medium-carbon steel, Scr. Mater. 74 (2014) 56–59. https://doi.org/10.1016/j.scriptamat.2013.10.019.